Analytic model for the bispectrum of galaxies in redshift space

Robert E. Smith,[1,2,*] Ravi K. Sheth,[1,+] and Román Scoccimarro[3,‡]

[1]*University of Pennsylvania, 209 South 33rd Street, Philadelphia, Pennsylvania 19104, USA*
[2]*Institute for Theoretical Physics, University of Zurich, Zurich, CH8051, Switzerland*
[3]*CCPP, Department of Physics, New York University, New York, New York 10003, USA*

(Received 18 December 2007; published 18 July 2008)

We develop an analytic theory for the redshift space bispectrum of dark matter, haloes, and galaxies. This is done within the context of the halo model of structure formation, as this allows for the self-consistent inclusion of linear and nonlinear redshift-space distortions and also for the nonlinearity of the halo bias. The model is applicable over a wide range of scales: on the largest scales the predictions reduce to those of the standard perturbation theory (PT); on smaller scales they are determined primarily by the nonlinear virial velocities of galaxies within haloes, and this gives rise to the U-shaped anisotropy in the reduced bispectrum—a finger print of the Finger-Of-God distortions. We then confront the predictions with measurements of the redshift-space bispectrum of dark matter from an ensemble of numerical simulations. On very large scales, $k = 0.05h$ Mpc^{-1}, we find reasonably good agreement between our halo model, PT and the data, to within the errors. On smaller scales, $k = 0.1h$ Mpc^{-1}, the measured bispectra differ from the PT at the level of $\sim$10%–20%, especially for colinear triangle configurations. The halo model predictions improve over PT, but are accurate to no better than 10%. On smaller scales $k =$ 0.5–1.0h Mpc^{-1}, our model provides a significant improvement over PT, which breaks down. This implies that studies which use the lowest order PT to extract galaxy bias information are not robust on scales $k \gtrsim 0.1h$ Mpc^{-1}. The analytic and simulation results also indicate that there is *no* observable scale for which the configuration dependence of the reduced bispectrum is constant—hierarchical models for the higher-order correlation functions in redshift space are unlikely to be useful. It is hoped that our model will facilitate extraction of information from large-scale structure surveys of the Universe, because different galaxy populations are naturally included into our description.

DOI: 10.1103/PhysRevD.78.023523 PACS numbers: 98.80.−k

I. INTRODUCTION

Statistical analyses of the large-scale structures observed in galaxy surveys can provide a wealth of information about the cosmological parameters, the underlying mass distribution, and the initial conditions of the Universe [1–5]. Some complex combination of the information is commonly extracted through measurement of the 2-point correlation function, or its Fourier space analogue the power spectrum. Since the evolved density field of galaxies is highly non-Gaussian, further complementary information is contained within the higher-order clustering statistics [6,7]. For example, analysis of the large-scale 3-point correlation function, or its Fourier space dual the bispectrum, on large scales, can: test the nonlinearity of bias—the way in which an observable tracer distribution samples the unobservable distribution of physical interest [8–11]; constrain our hypothesis of Gaussianity in the initial conditions [12–15]; break degeneracies between parameters, hence allowing improved constraints on the amplitude of the matter power spectrum. In addition, higher-order statistics have been highlighted as an important piece of solving the puzzle as to whether the observed accelerated expansion of the Universe is due to dark energy physics or a modification to gravity [16–19]. On smaller scales these statistics can be most usefully used as a discriminator for the shapes of haloes [20]—and thus have the potential to constrain the small-scale dark matter physics.

The current state of the art galaxy redshift surveys [21–24] have provided large samples of the Universe, and investigators have already carried out some of the tests noted above: 3-point correlation functions have been estimated by [25–30] and bispectra by [31–34].

The recovery of precise cosmological information from these measurements is not straightforward, owing to the influence of nonlinear mass evolution, biasing, and redshift-space distortions. Current theoretical modeling of the large-scale bispectrum rests on results from perturbation theory and nonlinear biasing in real (as opposed to redshift) space. In the large-scale limit, this gives rise to a simple model [8–10]:

$$Q^{\rm g}(k_1, k_2, \theta_{12}) = \frac{1}{b_1^{\rm g}}[Q^{\rm m}(k_1, k_2, \theta_{12}) + c_2^{\rm g}]; \qquad (1)$$

where the functions Q^i are the reduced bispectra of galaxies and matter, $Q^i_{123} \equiv B^i_{123}/[P^i_1 P^i_2 + P^i_2 P^i_3 + P^i_3 P^i_1]$. In the above $B_{123} \equiv B(k_1, k_2, \theta_{12})$ is the matter bispectrum

*res@physik.unizh.ch
+shethrk@physics.upenn.edu
‡rs123@nyu.edu

and $P_a \equiv P(k_a)$ the matter power spectrum. The coefficient b_1^g is the large-scale linear bias parameter and $c_2^g \equiv b_2^g/b_1^g$ is the first nonlinear bias parameter. It is usually assumed that this relation holds in redshift space as well, but that it does not in detail can be seen from the work of [35]. That it nevertheless appears to be a reasonable working hypothesis was demonstrated by [36]. We shall, hereafter, refer to this model in real and redshift space as PT and PTs, respectively.

There are several reasons why we wish to improve upon PTs. First, it is well known that in redshift space the distortion effects from nonlinear structures, such as Finger-of-God (hereafter FOG) distortions, pollute the scales that are usually identified for linear treatment. This cannot be accounted for in the perturbation theory in any other way than supposing *ad hoc* fixes to the model [35,37]. A pragmatist might argue that one may take scales that are sufficiently large that these corrections can be neglected. However, even if we are proficient enough to accurately separate linear from nonlinear scales, then we are still faced with losing a significant amount of information from our data through the restrictions to very large scales. Therefore some means for robustly modeling the FOG effects is clearly of great value as this may allow us to expand the utility of our data set and improve precision.

Second, in our study of the large-scale galaxy power spectrum [38] we found that there was nontrivial scale dependence arising from nonlinear bias and gravitational mode coupling, even on the largest scales currently probed. One may then ask how these properties affect the predicted bispectra.

Third, if we assume that galaxy velocity field is an unbiased tracer for the velocity field of dark matter, then through studying the higher-order clustering statistics in redshift space we have a direct probe of the statistical information of the dynamics of the cold dark matter (CDM) density field itself [39–42].

In this paper we build a new analytic model for the fully nonlinear redshift-space bispectrum. We will concentrate on the isotropically averaged (i.e. the monopole) bispectrum, for reasons of simplicity. We work in the context of the halo model [43], since it naturally affords a means for including linear and nonlinear density and velocity information [44–48] and neatly allows for the inclusion of galaxies [44,49–53]. Furthermore, as was shown in [38] the halo model presents a natural framework for understanding the origins of the nonlinear scale dependence of bias. However, the limitations of the halo model predictions for precision measurements of the matter power spectrum on large scales have been known for some time now [43,54–56]. We will therefore use measurements from numerical simulations to confirm the validity of our predictions.

The paper breaks up as follows: In Sec. II we formalize the halo model in redshift space, providing general expressions for the 3-point function and bispectrum. Section III details the necessary components of the model; we pay special attention to the redshift-space clustering of halo centers. Section IV presents the central analytic result of the paper—a calculation of the bispectrum monopole. Some results of evaluating our expressions are presented in Sec. V. In Sec. VI we confront our model with measurements from N-body simulations. In Sec. VII we summarize our conclusions.

Although our analysis is general, we shall illustrate our results with specific examples. When necessary, we assume a flat Friedmann-Lemaître-Robertson-Walker (FLRW) cosmological model with energy density at late times dominated by a cosmological constant (Λ) and a sea of collisionless cold dark matter particles as the dominant mass density. We set $\Omega_m = 0.27$ and $\Omega_\Lambda = 0.73$, where these are the ratios of the energy density in matter and a cosmological constant to the critical density, respectively. We use a linear theory power spectrum generated from `cmbfast` [57], with baryon content of $\Omega_b = 0.046$ and $h = 0.72$. The normalization of fluctuations is set through $\sigma_8 = 0.9$, which is the root-mean-square (r.m.s.) variance of fluctuations in spheres of radius $8h^{-1}$ Mpc.

II. HALO MODEL IN REDSHIFT SPACE

A. Formalism

In the halo model (see [43] for a review) the density field is decomposed into a set of dark matter haloes, where a halo is defined to be a region that has undergone gravitational collapse forming a dense virialized ball of CDM. All statistical quantities of interest are then considered as sums over the halo distribution. Thus to understand the large-scale clustering of a distribution of objects, haloes, galaxies, or dark matter, we simply require understanding of how the haloes themselves cluster; the different tracer types simply act as weights. In particular, different galaxy populations ''weight'' haloes differently: the halo occupation distribution (HOD) [49–53] specifies how the probability for obtaining N galaxies depends on halo mass M. To model redshift-space statistics, we require additional information about how the large-scale velocity field modifies the halo clustering, as well as a model for the distribution function of galaxy velocities within each halo. The halo model in redshift space, at the 2-point level, was developed by [45–47] (hereafter we shall refer to the halo model in real and redshift space as HM and HMs, respectively). However, some unresolved issues remained with regard to the base formalism. These were resolved by [48] and our description of 3-point statistics presented here extends these analyses. For completeness some of these details are repeated below. Before continuing, we note that the problem of redshift-space distortions in the halo model was also recently addressed by [58], who used numerical simulations to construct an empirical model for the distribution function of halo pairwise velocities. Our approach is complimentary to that, since the results for the large-scale halo

clustering are derived within the context of the analytic perturbation theory rather than being fit for.

The density field of dark matter, haloes, or galaxies may be written as

$$\rho^s_\alpha(\mathbf{s}) = \sum_i [W_\alpha]_i U^s_{\alpha,i}(\mathbf{s} - \mathbf{s}_i|M_i), \tag{2}$$

where $\alpha = \{1, 2, 3\}$ refers to the particular choice of weight for the ith halo in the sum, i.e. $[W_\alpha]_i = \{1, M_i, N^{\rm g}(M_i), \ldots\}$ depending on the spectra one wishes to model, and where $N^{\rm g}(M_i)$ is the number of galaxies in halo i. $U^s_{\alpha,i}$ is the normalized density distribution of objects in redshift space within the ith halo. In this paper we shall always assume that $U^s_{\alpha,i} \equiv \rho^s(\mathbf{s})/M$, is the mass-normalized density profile of dark matter in redshift space, although our formalism does not rely upon this assumption and may readily be generalized for more complicated mass distributions. At this point the only difference between Eq. (2) and the real-space density field is that we have used $\mathbf{s}$ to denote comoving spatial positions. However this has the special meaning that Hubble's law, $\mathbf{v} = H(a)\mathbf{r}$, is used to infer proper radial positions from recession velocities, where $\mathbf{v}$ is the proper velocity, $H(a) \equiv \dot{a}/a$ is the Hubble parameter, and $\mathbf{r}$ is the proper separation (related to comoving coordinate through $\mathbf{r} = a\mathbf{x}$). The notion of redshift-space distortions then follows from the fact that objects which form through gravitational instability acquire a local peculiar velocity of their own, and hence the velocity-space mapping in general is nonlinear. In this paper we shall work in *the plane parallel approximation*, where observed structures are located at infinity. Then the mapping is

$$s_z = z - u_z(\mathbf{x}); \qquad \mathbf{s}_\perp = \mathbf{x}_\perp, \tag{3}$$

where the Cartesian components of the position vectors have been written $(\mathbf{x}_\perp, z)$, with $\mathbf{x}_\perp = (x, y)$. Thus s_z and u_z specify the z-components of the redshift-space position vector $\mathbf{s}$ and the comoving peculiar velocity field $\mathbf{u}$, scaled in units of the Hubble parameter, respectively. Note that we take $\mathbf{u}$ to be negative for convenience.

B. Higher-order correlations

We may now compute the correlation hierarchy for such a distribution of tracer objects. For a definition of the higher-order clustering statistics in configuration space and their Fourier space dual counterparts we refer to Appendix A. There may also be found useful symmetry properties that we exploit throughout.

Following [20,43,52,59,60], the real-space 3-point correlation function (ζ^s_α) in the halo model, for dark matter, haloes, or galaxies, is the sum of three terms: the first represents the case where all three points in space are contained in a single halo; the second is the case where two points are located in one halo, and the third is in a separate halo; the third is the case where three points are located in three distinct haloes—we shall refer to these as the 1-, 2-, and 3-halo terms and $(\zeta^s_{\alpha,1\rm H}, \zeta^s_{\alpha,2\rm H}, \zeta^s_{\alpha,3\rm H})$. These are written:

$$\zeta^s_\alpha(\mathbf{s}_1, \mathbf{s}_2, \mathbf{s}_3) \equiv \zeta^s_{\alpha,1\rm H}(\mathbf{s}_1, \mathbf{s}_2, \mathbf{s}_3) + \zeta^s_{\alpha,2\rm H}(\mathbf{s}_1, \mathbf{s}_2, \mathbf{s}_3) + \zeta^s_{\alpha,3\rm H}(\mathbf{s}_1, \mathbf{s}_2, \mathbf{s}_3); \tag{4}$$

$$\zeta^s_{\alpha,1\rm H}(\mathbf{s}_1, \mathbf{s}_2, \mathbf{s}_3) = \frac{1}{\bar{\rho}^3_\alpha} \int dM d^3y [W_\alpha]^3 n(M) \times \prod_{i=1}^{3} \{U^s(\mathbf{y} - \mathbf{s}_i|M)\}; \tag{5}$$

$$\zeta^s_{\alpha,2\rm H}(\mathbf{s}_1, \mathbf{s}_2, \mathbf{s}_3) = \frac{1}{\bar{\rho}^3_\alpha} \int \prod_{i=\{1,2\}} \{dM_i d^3y_i [W_\alpha]_i n(M_i) \times U^s(\mathbf{y}_i - \mathbf{s}_i|M_i)\} [W_\alpha]_1 U^s(\mathbf{y}_1 - \mathbf{s}_3|M_1) \times \xi^s_{\rm hc}(\mathbf{y}_1, \mathbf{y}_2|M_1, M_2) + \text{cyc}; \tag{6}$$

$$\zeta^s_{\alpha,3\rm H}(\mathbf{s}_1, \mathbf{s}_2, \mathbf{s}_3) = \frac{1}{\bar{\rho}^3_\alpha} \int \prod_{i=1}^{3} \{dM_i d^3y_i [W_\alpha]_i n(M_i) \times U^s(\mathbf{y}_i - \mathbf{s}_i|M_i)\} \times \zeta^s_{\rm hc}(\mathbf{y}_1, \mathbf{y}_2, \mathbf{y}_3|M_1, M_2, M_3), \tag{7}$$

where $\xi^s_{\rm hc}$ and $\zeta^s_{\rm hc}$ are the 2- and 3-point correlation functions of halo centers, conditioned on halo masses and where $n(M)dM$ is the halo mass function, which gives the number density of dark matter haloes with masses in the range M to $M + dM$.

The inverse Fourier transforms of these 3-point functions are the redshift-space bispectra (cf. Eq. (A18)). They are written:

$$B^s_\alpha(\mathbf{k}_1, \mathbf{k}_2, \mathbf{k}_3) = B^s_{\alpha,1\rm H}(\mathbf{k}_1, \mathbf{k}_2, \mathbf{k}_3) + B^s_{\alpha,2\rm H}(\mathbf{k}_1, \mathbf{k}_2, \mathbf{k}_3) + B^s_{\alpha,3\rm H}(\mathbf{k}_1, \mathbf{k}_2, \mathbf{k}_3), \tag{8}$$

$$B^s_{\alpha,1\rm H}(\mathbf{k}_1, \mathbf{k}_2, \mathbf{k}_3) = \frac{1}{\bar{\rho}^3_\alpha} \int dM [W_\alpha]^3 n(M) \prod_{i=1}^{3} \{U^s(\mathbf{k}_i|M)\}, \tag{9}$$

$$B^s_{\alpha,2\rm H}(\mathbf{k}_1, \mathbf{k}_2, \mathbf{k}_3) = \frac{1}{\bar{\rho}^3_\alpha} \times \int \prod_{i=\{1,2\}} \{dM_i [W_\alpha]_i n(M_i) U^s(\mathbf{k}_i|M_i)\} \times [W_\alpha]_1 U^s(\mathbf{k}_3|M_1) P^s_{\rm hc}(\mathbf{k}_2|M_1, M_2) + \text{cyc}, \tag{10}$$

$$B^s_{\alpha,3\mathrm{H}}(\mathbf{k}_1,\mathbf{k}_2,\mathbf{k}_3)=\frac{1}{\bar{\rho}^3_\alpha}\int\prod_{i=1}^{3}\{dM_i[W_\alpha]_i n(M_i)U^s(\mathbf{k}_i|M_i)\}B^s_{\mathrm{hc}}(\mathbf{k}_1,\mathbf{k}_2,\mathbf{k}_3|M_1,M_2,M_3), \tag{11}$$

where P^s_{hc} and B^s_{hc} are the Fourier transforms of the 2- and 3-point halo center correlation functions.

Several advantages are gained from transforming to Fourier space. First, once the integrals over mass are included, $\zeta^s_{3\mathrm{H}}$ requires evaluation of a 12-D integral—the corresponding term $B^s_{3\mathrm{H}}$ is significantly simpler. Indeed, for the case of real space—not redshift space—and for spherical haloes, it is possible to write $B_{3\mathrm{H}}$ as the product of 3 2-D integrals. The calculation is slightly more complicated in redshift space but, as we show below, it remains tractable. Thus, to compute the redshift-space power spectrum and bispectrum, we require three components: the abundance of dark matter haloes $n(M)$; a model for the redshift-space density profile; and a model for the interclustering of dark matter haloes in redshift space. In the following sections we describe our choices for these quantities.

III. INGREDIENTS

A. Halo abundances and bias factors

The halo mass function $n(M)$ plays a central role in the halo model. It has been the subject of much detailed study [61–64]. These studies suggest that, in appropriately scaled units, halo abundances should be approximately independent of cosmology, power spectrum, and redshift. These models for $n(M)$ also predict that the real-space clustering of halos should be biased relative to that of the dark matter [63]; the way in which real-space halo bias depends on halo mass is related to the shape of $n(M)$. Thus, once the mass function has been specified, the problem of describing halo clustering reduces to one of describing the clustering of the dark matter. Of the many recent parametrizations of $n(M)$, [63,65–67], we use that of Sheth and Tormen [63]. Changing to that of Warren *et al.* [66] for instance, does not affect the large-scale matter predictions and changes the results in the nonlinear regime by a few percent. Note that for the bispectrum, as was shown by [52], a more important issue to be aware of is the finite volume effect, which can significantly change the measured statistics for small volumes. The halo bias factors associated with this mass function are reported in [52]; we use these in what follows. Reference [38] describes other empirical approaches to determining halo bias parameters.

B. Density profiles in redshift space

Consider the 6-D phase-space density distribution function for dark matter particles within a particular halo, denoted $\mathcal{F}(\mathbf{x},\mathbf{u}|M)$. The density profile and velocity distribution function may be obtained by marginalizing over velocities and positions, respectively:

$$\begin{aligned}\rho(\mathbf{x})&=M\int d\mathbf{u}\,\mathcal{F}(\mathbf{x},\mathbf{u}|M);\\ \mathcal{V}_{3\mathrm{D}}(\mathbf{u})&=\int d\mathbf{x}\,\mathcal{F}(\mathbf{x},\mathbf{u}|M),\end{aligned} \tag{12}$$

where M is the normalizing mass. The redshift-space density profile can be readily obtained from the phase-space distribution through transformation to the new random variable $\mathbf{s}$, given by our fundamental mapping (Eq. (3)). Hence

$$\begin{aligned}\rho^s(\mathbf{s}_\perp,s_z)&=M\int dz d\mathbf{x}_\perp du_z d\mathbf{u}_\perp\mathcal{F}(\mathbf{x}_\perp,z,\mathbf{u}_\perp,u_z|M)\\&\quad\times\delta^D(s_z-z+u_z)\delta^D(\mathbf{s}_\perp-\mathbf{x}_\perp),\\&=M\int dz d\mathbf{u}_\perp\mathcal{F}(\mathbf{s}_\perp,z,\mathbf{u}_\perp,z-s_z|M).\end{aligned} \tag{13}$$

We now assume that the density distribution of matter within each halo can be described by a spherically symmetric density profile and that the particle orbits are isotropic and independent of position within the halo, i.e. an isothermal velocity distribution. Thus, the phase-space distribution is separable, i.e. $\mathcal{F}(\mathbf{x},\mathbf{u}|M)=\rho(\mathbf{x}|M)\times\mathcal{V}_{3\mathrm{D}}(\mathbf{u}|M)/M$. Since the velocity distribution function is isotropic it may now be written as the product of three independent distributions in the three coordinate directions: $\mathcal{V}_{3\mathrm{D}}(\mathbf{u}|M)=\mathcal{V}_{1\mathrm{D}}(u_x|M)\mathcal{V}_{1\mathrm{D}}(u_y|M)\mathcal{V}_{1\mathrm{D}}(u_z|M)$; and we shall hereafter use the notation that $\mathcal{V}_{1\mathrm{D}}\equiv\mathcal{V}$. Hence,

$$\rho^s(\mathbf{s}_\perp,s_z|M)=\int dz\rho(\mathbf{s}_\perp,z|M)\mathcal{V}(s_z-z|M). \tag{14}$$

Fourier transforming yields the compact expression

$$U^s(\mathbf{k}_\perp,k_z|M)=U(k|M)\mathcal{V}(\mu k|M), \tag{15}$$

where $\mathbf{k}_\perp$ denotes a 2-D wave vector perpendicular to the distortion, and $k_z=\mu k=\mathbf{k}\cdot\hat{\mathbf{z}}$ is parallel to it.

This expression shows that the redshift-space profile is anisotropic because the spherically symmetric real-space profile U has been convolved along the line-of-sight direction with displacements generated by the velocity distribution $\mathcal{V}$. That is to say, $\mathcal{V}$ is the quantity in the model which generates FOG distortions and since it represents virial motions, it is clearly the sort of nonlinear effect that PTs based approaches must model *ad hoc*. We also note that if $\mathcal{V}$ makes the redshift profile substantially anisotropic, then these nonlinear effects may extend farther into the linear regime than one might otherwise have expected.

We caution that this simple model of the halo phase space will almost certainly not be strictly valid, since it clearly neglects many aspects of the more complex physics

that we understand to play an important role for the internal dynamics of haloes [68]. Nevertheless, previous studies have shown that the isothermal model appears to be a reasonable approximation when ensemble average quantities are considered [69]. However, as we show in Appendix B this model does not provide a robust description of the 1-D velocity dispersion mass relation for haloes in our simulations. We have therefore introduced a parameter ϵ into the modeling, that will be used to account for any small departures away from isothermality (see Sec. VI B for additional discussion).

Precise details of the models we employ for the density profile and for the 1-point distribution function of velocities are presented in Appendix B. Note also that owing to the density profile and mass function model employing different conventions for the halo mass, we must convert between them, and we do this using the procedure from [70] (see also Appendix B 2).

C. Halo center clustering in redshift space

On large scales the success of our analytic model will primarily be determined by its ability to reproduce the large-scale clustering of the halo centers. For this we use the redshift-space halo-PT developed in [48], which is accurate up to the 1-loop level in perturbation theory. The main result we draw from that work is the idea that the halo density field may be written as perturbation series that involves the standard density PT kernels [6] and the nonlinear bias parameters [8]. Explicitly we have the series

$$\delta^s_{\rm hc}(\mathbf{k}, a|M, R) = \sum_{n=0}^{\infty} [D_1(a)]^n [\delta^s_{\rm hc}(\mathbf{k}|M, R)]_n, \tag{16}$$

$$[\delta^s_{\rm hc}(\mathbf{k}|M, R)]_n = \int \prod_{i=1}^{n} \left\{ \frac{d^3 q_i}{(2\pi)^3} \delta_1(\mathbf{q}_i) \right\} (2\pi)^3 \times [\delta^D(\mathbf{k})]_n Z^{\rm hc}_n(\mathbf{q}_1, \ldots, \mathbf{q}_n|M, R), \tag{17}$$

where $D(t)$ is the linear theory growth function and $f(\Omega) \equiv d\ln D(a)/d\ln a$ is the logarithmic growth rate of the velocity field. The functions $Z^{\rm hc}_n(\mathbf{q}_1, \ldots, \mathbf{q}_n|M, R)$ are the redshift-space halo-PT kernels symmetrized in all of their arguments and we make explicit their dependencies on halo mass and the scale over which the density field has been smoothed. Kernels up to second order are [35,37,71]:

$$Z^{\rm hc}_0 = F^{\rm hc}_0 \equiv b_0; \tag{18}$$

$$Z^{\rm hc}_1 = F^{\rm hc}_1 + f(\Omega)\mu_1^2 \tilde{G}_1[1 + b_0]; \tag{19}$$

$$Z^{\rm hc}_{1,2} = F^{\rm hc}_{1,2} + f(\Omega)\mu^2_{12}\tilde{G}_{1,2} + \frac{1}{2} f(\Omega)\mu_{12}k_{12}\left\{ \frac{\mu_1}{q_1}\tilde{G}_1[F^{\rm hc}_2 + f(\Omega)\mu_2^2\tilde{G}_2] + \frac{\mu_2}{q_2}\tilde{G}_2[F^{\rm hc}_1 + f(\Omega)\mu_1^2\tilde{G}_1] \right\} + \frac{1}{2}[f(\Omega)\mu_{12}k_{12}]^2 \frac{\mu_1}{q_1}\frac{\mu_2}{q_2}\tilde{G}_1\tilde{G}_2 b_0, \tag{20}$$

where we have adopted the short-hand notation:

$$Z^{\rm hc}_{i_1,\ldots,i_n} \equiv Z^{\rm hc}_n(\mathbf{q}_{i_1}, \ldots, \mathbf{q}_{i_n}|M, R);$$
$$F^{\rm hc}_{i_1,\ldots,i_n} \equiv F^{\rm hc}_n(\mathbf{q}_{i_1}, \ldots, \mathbf{q}_{i_n}|M, R);$$
$$\tilde{G}_{i_1,\ldots,i_n} \equiv W(|\mathbf{q}_{i_1} + \cdots + \mathbf{q}_{i_n}|R) G_n(\mathbf{q}_{i_1}, \ldots, \mathbf{q}_{i_n});$$

and where

$$\mu_{i_1\ldots i_n} \equiv \frac{(\mathbf{q}_{i_1} + \cdots + \mathbf{q}_{i_n}) \cdot \hat{\mathbf{z}}}{k_{i_1\ldots i_n}}; \tag{21}$$

$$k_{i_1\ldots i_n} \equiv |\mathbf{q}_{i_1} + \cdots + \mathbf{q}_{i_n}|. \tag{22}$$

The quantities $F^{\rm hc}_n$ are the nth order halo-PT kernels (see Appendix C and [38] for complete details). The functions G_n represent the nth order Eulerian PT kernels for the divergence of the velocity field [6]. Note that these expressions are almost identical to the redshift-space PT kernels derived by [35,37], however they differ in some subtle ways: one, we have explicitly included their dependence on the smoothing filter $W(q)$, which is needed to facilitate the Taylor expansion; and two, we are applying this in the context of haloes and not galaxies and so they depend on the nonlinear halo bias parameters $b_i(M)$, instead of the nonlinear galaxy bias parameters (see discussion in Sec. III A). Note that we have also included $b_0(M)$, since this does not have to be zero, although we will take it to be so for all our later analysis.

Following standard methods for calculating polyspectra, we find that the halo center bispectrum, $B^s_{\rm hc,123} \equiv B^s_{\rm hc}(\mathbf{k}_1, \mathbf{k}_2, \mathbf{k}_3|M_1, M_2, M_3, R)$, up to fourth order in the redshift-space halo-PT, is

$$B^s_{\rm hc,123} = 2P_{11}(k_1)P_{11}(k_2)Z^{\rm hc}_1(\mathbf{k}_1|M_1, R)Z^{\rm hc}_1(\mathbf{k}_2|M_2, R) \times Z^{\rm hc}_2(\mathbf{k}_1, \mathbf{k}_2|M_3, R) + 2\,\text{cyc.} \tag{23}$$

Inserting our expressions for the redshift-space halo-PT kernels, Eqs. (18)–(20), into the above expression, reveals

$$\frac{B^s_{\rm hc,123}(M_1,M_2,M_3)}{W(k_1R)W(k_2R)W(k_3R)} = 2b_1(M_1)b_1(M_2)b_1(M_3)P_{11}(k_1)P_{11}(k_2)\prod_{i=1,2}\{1+\beta_i\mu_i^2[1+b_0(M_i)]\}\Big[F_2(\mathbf{k}_1,\mathbf{k}_2) + \beta_3\mu_{12}^2 G_2(\mathbf{k}_1,\mathbf{k}_2) + \frac{W(k_1R)W(k_2R)}{W(k_3R)}\Big(\frac{c_2(M_3)}{2} + \frac{1}{2}[f(\Omega)\mu_{12}k_{12}]^2\frac{\mu_1}{k_1}\frac{\mu_2}{k_2}c_0(M_3) + \frac{1}{2}f(\Omega)\mu_{12}k_{12}\Big\{\frac{\mu_1}{k_1}[1+\beta_3\mu_2^2] + \frac{\mu_2}{k_2}[1+\beta_3\mu_1^2]\Big\}\Big)\Big] + 2\,\text{cyc.}, \tag{24}$$

where $\beta_i \equiv f(\Omega)/b_1(M_i)$ and where $c_j(M_i) = b_j(M_i)/b_1(M_i)$. As in our real-space work on the power spectrum, we are now faced with the situation that we have solved for the bispectrum of halo centers filtered on scale R, and in fact we would like to recover the unfiltered bispectrum. As in [38], we take the following *ansatz*: the filtering of the spectra can be reversed through the following operation:

$$P(\mathbf{k}) \equiv \frac{P(\mathbf{k}|R)}{W^2(kR)}; \qquad B(\mathbf{k}_1,\mathbf{k}_2,\mathbf{k}_3) \equiv \frac{B(\mathbf{k}_1,\mathbf{k}_2,\mathbf{k}_3|R)}{W(k_1R)W(k_2R)W(k_3R)} \tag{25}$$

and this explains the form of the left-hand side of Eq. (24). An alternative approach to the filtering issue for the power spectrum and bispectrum was proposed by [72], we shall leave the solution of this problem for future consideration.

With these ingredients prepared, we are now in full possession of a complete description of the bispectrum of galaxies, haloes, and dark matter in the halo model and in the presence of a local, nonlinear scale dependent bias. In the next section we develop these equations further.

IV. THE BISPECTRUM MONOPOLE

A. Euler angle averages

The redshift-space bispectrum is an anisotropic function on the sphere that depends on 5 variables. The first three are the triangle configuration, and the other two specify its orientation with respect to the z-axis. However, it is common practice to measure this quantity averaged over all possible orientations of the coordinate frame. Thus to compare with this isotropized observable, we shall now derive the isotropized form for the halo model, which we shall denote $\bar{B}^s$. Interestingly, the following approach is identical to that which one performs for the triaxial halo model in real space [20,70], since on small scales, one may effectively think of transforming to redshift space as simply transforming a set of spherical haloes into a set of prolate ellipsoids whose semimajor axes all point along the line of sight. Of course, the real situation is more complex, since the halo centers are also distorted according to the halo velocity projected along the line of sight, but nevertheless we may borrow some mathematical machinery from the triaxial halo analysis.

The isotropic function is thus

$$\bar{B}^s(k_1,k_2,\theta_{12}) = \frac{1}{8\pi^2}\int d\gamma_1 d(\cos\gamma_2)d\gamma_3 B^s[\mathcal{R}(\gamma_1,\gamma_2,\gamma_3)\mathbf{k}_1, \mathcal{R}(\gamma_1,\gamma_2,\gamma_3)\mathbf{k}_2], \tag{26}$$

where $\mathcal{R}(\gamma_1,\gamma_2,\gamma_3)$ is the rotation matrix for the components of the basis vectors. $\mathcal{R}(\gamma_1,\gamma_2,\gamma_3)$ is parametrized by three position or Euler angles, $(\gamma_1,\gamma_2,\gamma_3)$ and these are the $z'-y'-z''$ rotation angles (see Appendix D for the explicit form of the matrix we use). Note that we assign uniform probability on the sphere to each triple of angles.

The following considerations simplify this expression considerably. First, in the PT expressions for B^s, each term depends on either the angle between two k-vectors or the projection of each vector along the z-axis. In the first case, the use of matrix notation shows that

$$[\mathbf{k}_i']^T\mathbf{k}_j' = [\mathcal{R}(\gamma_1,\gamma_2,\gamma_3)\mathbf{k}_i]^T\mathcal{R}(\gamma_1,\gamma_2,\gamma_3)\mathbf{k}_j = \mathbf{k}_i^T\mathcal{R}(\gamma_1,\gamma_2,\gamma_3)^T\mathcal{R}(\gamma_1,\gamma_2,\gamma_3)\mathbf{k}_j = \mathbf{k}_i^T\mathbf{k}_j; \tag{27}$$

this is the well-known result that scalar products are invariant under rotations of the coordinate basis functions. In the second case, the projection of each rotated vector onto the line-of-sight direction (or z-axis) can be written

$$\mathbf{k}'\cdot\hat{\mathbf{z}} = \mathcal{R}(\gamma_1,\gamma_2,\gamma_3)\mathbf{k}\cdot\hat{\mathbf{z}} = k_x\sin\gamma_2\cos\gamma_1 + k_y\sin\gamma_2\sin\gamma_1 + k_z\cos\gamma_2 \equiv A(\mathbf{k},\gamma_1,\gamma_2), \tag{28}$$

Thus, we see that the resultant function must be invariant under the γ_3 rotation, and hence this integral may be computed trivially. Finally, because our final quantity $\bar{B}$ must be independent of the initial locations of the k-vector triple, we may without loss of generality choose these locations to be as convenient as possible. Therefore, we let the initial $\mathbf{k}_1$ vector lies along the polar axis and constrain $\mathbf{k}_2$ and $\mathbf{k}_3$ to lie in the z-y plane: i.e.

$$[\mathbf{k}_1]^T = (0,0,k_1), \qquad [\mathbf{k}_2]^T = (0,k_2\cos\theta_{12},k_2\sin\theta_{12}), \qquad [\mathbf{k}_3]^T = (0,-k_2\cos\theta_{12},-k_1-k_2\sin\theta_{12}), \tag{29}$$

where the last equality uses the closure condition: $\sum_i \mathbf{k}_i = 0$. Thus, the k-vectors rotated into the new basis and dotted with the z-direction are now written:

$$\begin{aligned} A_1 &= \cos\gamma_2 (k_1)_z; \\ A_2 &= \sin\gamma_2 \sin\gamma_1 (k_2)_y + \cos\gamma_2 (k_2)_z; \\ A_3 &= -\sin\gamma_2 \sin\gamma_1 (k_2)_y - \cos\gamma_2 [(k_1)_z + (k_2)_z]. \end{aligned} \tag{30}$$

The parameters $A_i \equiv A(\mathbf{k}_i, \gamma_1, \gamma_2)$ are simply related to the cosines of the k-vectors along the z-axis:

$$\mu_1 = \frac{A_1}{k_1}; \qquad \mu_2 = \frac{A_2}{k_2}; \qquad \mu_3 = -\mu_1 \frac{k_1}{k_3} - \mu_2 \frac{k_2}{k_3}, \tag{31}$$

where $q \equiv k_2/k_1$.

We may now apply the above operation directly to our expressions for the anisotropic bispectrum (Eqs. (9)–(11)). On inserting the A_i into each instance of μ_i in the density profiles (Eq. (15)) and the halo center power spectra and bispectrum (Eqs. (E4) and (24)), we find that the 1-, 2-, and 3-halo terms for the bispectrum monopole become

$$\bar{B}^{\,s}_{1\mathrm{H}}(k_1, k_2, \theta_{12}) = \frac{1}{4\pi \bar{\rho}_\alpha^3} \int d\gamma_1 d(\cos\gamma_2) \int dM [W_\alpha]^3 n(M) \prod_{i=1}^{3} \{U(k_i|M) \mathcal{Y}(\mu_i k_i|M)\}; \tag{32}$$

$$\begin{aligned} \bar{B}^{\,s}_{2\mathrm{H}}(k_1, k_2, \theta_{12}) = \frac{1}{4\pi \bar{\rho}_\alpha^3} \int d\gamma_1 d(\cos\gamma_2) \prod_{i=\{1,2\}} \left\{ \int dM_i [W_\alpha]_i b_1(M_i) n(M_i) U(k_i|M_i) \mathcal{Y}(\mu_i k_i|M_i) \right\} \\ \times [W_\alpha]_1 U(k_3|M_1) \mathcal{Y}(\mu_3 k_3|M_1) P_{11}(k_2) \{1 + [\beta_1 + \beta_2]\mu_2^2 + \beta_1 \beta_2 \mu_2^4\} + \mathrm{cyc}; \end{aligned} \tag{33}$$

$$\begin{aligned} \bar{B}^{\,s}_{3\mathrm{H}}(k_1, k_2, \theta_{12}) = \frac{1}{4\pi \bar{\rho}_\alpha^3} \int d\gamma_1 d(\cos\gamma_2) \\ \times \prod_{i=1}^{3} \left\{ \int dM_i [W_\alpha]_i n(M_i) U(k_i|M_i) \mathcal{Y}(\mu_i k_i|M_i) \right\} B^s_{\mathrm{hc}}(k_1, k_2, \theta_{12}, \mu_1, \mu_2|M_1, M_2, M_3). \end{aligned} \tag{34}$$

The only variables that depend on the Euler angles γ_1 and γ_2 are μ_i and A_i. Each term requires evaluation of no more than a 4-D embedded integral: two integrals for the Euler angles, one for the mass and one for the Fourier transform of the density profile. Note that for simplicity, we have kept only the leading order contribution to the 2-halo term. Technically this should be taken up to the 1-loop level to be consistent with the bispectrum which is 4th order in δ. However, this issue is beyond the scope of the current paper and will be addressed in [48].

B. Computational considerations

Our expressions for the bispectrum as presented above are complete. However some calculational effort is still required before we may attempt a practical implementation on the computer. We now present some simplifications.

We begin by defining some convenient notation: Let $\psi^{(i)}_{\delta,j}$ and $\psi_{v,j}$ denote the following integrals:

$$\begin{aligned} \psi^{(i)}_{\delta,j}(\mathbf{k}_1, \ldots, \mathbf{k}_j) = \frac{1}{\bar{\rho}_\alpha^j} \int dM n(M) b_i(M) \\ \times \prod_{l=1}^{j} \{[W_\alpha] U(k_l|M) \mathcal{Y}(\mu_l k_l|M)\}; \end{aligned} \tag{35}$$

$$\begin{aligned} \psi_{v,j}(\mathbf{k}_1, \ldots, \mathbf{k}_j) = \frac{f(\Omega)}{\bar{\rho}_\alpha^j} \int dM n(M) \\ \times \prod_{l=1}^{j} \{[W_\alpha] U(k_l|M) \mathcal{Y}(\mu_l k_l|M)\}. \end{aligned} \tag{36}$$

The first integral generalizes the halo bias weighting scheme applied to the density field for the situation where j-points are within a single halo. The second integral generalizes the weighting scheme to the similar situation for the halo velocity field. This notation has some similarities with that of [46], but is different in the way in which the velocity field is treated—recall that the velocity field has been assumed to be unbiased.

In this notation we may rewrite the 2- and 3-halo terms in the bispectrum; the 1-halo term requires no simplification. Through rearrangement of the mass integrals and expansion of the halo center power spectrum through substitution of the appropriate kernels, we find that the 2-halo term can now be written

$$\begin{aligned} \bar{B}^{\,s}_{\alpha,2\mathrm{H}}(k_1, k_2, \theta_{12}) = \frac{1}{4\pi} \int d\gamma_1 d(\cos\gamma_2) \{P(k_2) \\ \times [\psi^{(1)}_{\delta,2}(\mathbf{k}'_1, \mathbf{k}'_3) \psi^{(1)}_{\delta,1}(\mathbf{k}'_2) \\ + (\psi_{v,2}(\mathbf{k}'_1, \mathbf{k}'_3) \psi^{(1)}_{\delta,1}(\mathbf{k}'_2) \\ + \psi^{(1)}_{\delta,2}(\mathbf{k}'_1, \mathbf{k}'_3) \psi_{v,1}(\mathbf{k}'_2)) \mu_2^2 \\ + \psi_{v,2}(\mathbf{k}'_1, \mathbf{k}'_3) \psi_{v,1}(\mathbf{k}'_2) \mu_2^4] + 2\,\mathrm{cyc}\}. \end{aligned} \tag{37}$$

The 3-halo term is significantly more complex, owing to the halo center bispectrum being the product of two first order kernels and one second order kernel. Nevertheless, we may again isolate the integrals over mass and use the ψ functions to obtain

$$\bar{B}^{s}_{3\mathrm{H}}(k_1,k_2,\theta_{12}) = \frac{1}{4\pi}\int d\gamma_1 d(\cos\gamma_2)\Big\{2P(k_1)P(k_2)T_1(\mathbf{k}'_1,\mathbf{k}'_2)\Big[T_2(\mathbf{k}'_1,\mathbf{k}'_2|\mathbf{k}'_3)\psi^{(1)}_{\delta,1}(\mathbf{k}'_3) + T_3(\mathbf{k}'_1,\mathbf{k}'_2|\mathbf{k}'_3)\psi_{v,1}(\mathbf{k}'_3) + \mathcal{W}_{12,3}\frac{\psi^{(2)}_{\delta,1}(\mathbf{k}'_3)}{2} + T_4(\mathbf{k}'_1,\mathbf{k}'_2|\mathbf{k}'_3)\psi^{(0)}_{\delta,1}(\mathbf{k}'_3)\Big] + 2\,\mathrm{cyc}\Big\}; \tag{38}$$

where we have defined the following useful quantities:

$$T_1(\mathbf{k}_i,\mathbf{k}_j) = \prod_{m=i,j}\{\psi^{(1)}_{\delta,1}(\mathbf{k}_m) + \mu_m^2[\psi_{v,1}(\mathbf{k}_m) + f(\Omega)\psi^{(0)}_{\delta,1}(\mathbf{k}_m)]\}; \tag{39}$$

$$T_2(\mathbf{k}_i,\mathbf{k}_j|\mathbf{k}_l) = F_2(\mathbf{k}_i,\mathbf{k}_j) + \frac{1}{2}\mathcal{W}_{ij,l}f(\Omega)\mu_{ij}k_{ij}\times\left[\frac{\mu_i}{k_i}+\frac{\mu_j}{k_j}\right]; \tag{40}$$

$$T_3(\mathbf{k}_i,\mathbf{k}_j|\mathbf{k}_l) = \mu_{ij}^2 G_2(\mathbf{k}_i,\mathbf{k}_j) + \frac{1}{2}\mathcal{W}_{ij,l}f(\Omega)\mu_{ij}k_{ij}\left[\frac{\mu_i}{k_i}\mu_j^2+\frac{\mu_j}{k_j}\mu_i^2\right]; \tag{41}$$

$$T_4(\mathbf{k}_i,\mathbf{k}_j|\mathbf{k}_l) = \frac{1}{2}\mathcal{W}_{ij,l}[f(\Omega)\mu_{ij}k_{ij}]^2\frac{\mu_i}{k_i}\frac{\mu_j}{k_j}; \tag{42}$$

and

$$\mathcal{W}_{ij,l} \equiv \frac{W(k_iR)W(k_jR)}{W(k_lR)}. \tag{43}$$

The advantage of this reformulation of the 2- and 3-halo terms is that we have decomposed the integrand into a set of algebraic functions of the ψ integrals (Eqs. (35) and (36)), and auxiliary functions, and these may all be computed in parallel making the computation highly modular.

C. The large-scale limit

Next we consider the redshift-space bispectrum in the very large-scale limit, as this should asymptotically reduce to the standard PT expressions for the bispectrum, modulo discreteness corrections for the point process associated with the halo field. However, let us first examine the large-scale limit of Eqs. (35) and (36). On letting $\{\mathbf{k}_i\}\to 0$, the density profile terms become $U^s(\mathbf{k}_i)\to 1$, the window function becomes $\mathcal{W}_{ij,l}\to 1$, and so

$$\lim_{\{k_j\}\mapsto 0}\psi^{(i)}_{\delta,j} = \frac{\langle b_i(M)[W_\alpha]^j\rangle}{\langle[W_\alpha]\rangle^j}; \qquad \lim_{\{k_j\}\mapsto 0}\psi_{v,j} = \frac{f(\Omega)\langle[W_\alpha]^j\rangle}{\langle[W_\alpha]\rangle^j}; \tag{44}$$

where $\langle\ldots\rangle = \int dM p(M)\ldots$, with $p(M)\equiv n(M)/\bar{n}_{\mathrm{H}}$, $\bar{n}_{\mathrm{H}}$ being the total number density of haloes in the required mass range. When $j=1$ we write these functions more simply as: the average nonlinear bias parameter for the tracer particles, $\psi^{(i)}_{\delta,1}\equiv\bar{b}_{\alpha,i}$, and the logarithmic growth factor for the linear velocity field $\psi_{v,1}\equiv f(\Omega)$.

The bispectrum in the large-scale limit can now be computed directly. The 1-halo term is trivially obtained, and the 2- and 3-halo terms can be developed through replacing the ψ functions in the general expressions (37) and (38), for their large-scale forms (44). After some algebraic manipulation we arrive at the result

$$\bar{B}^{s}_{\alpha}(k_1,k_2,\theta_{12}) = \bar{B}^{s}_{\alpha,\mathrm{PT}}(k_1,k_2,\theta_{12}) + \frac{1}{\bar{n}_{\alpha,2\mathrm{H}}}[P(k_2)+P(k_3)+P(k_1)] + \frac{1}{\bar{n}^2_{\alpha,1\mathrm{H}}}; \tag{45}$$

where the large-scale PT bispectrum monopole in redshift space is given by

$$\bar{B}^{s}_{\alpha,\mathrm{PT}}(k_1,k_2,\theta_{12}) = \frac{1}{4\pi}\int d\gamma_1 d(\cos\gamma_2)\prod_{i=1,2}\{\bar{b}_{\alpha,1}+\mu_i^2 f(\Omega)[1+\bar{b}_{\alpha,0}]\}\Big\{2P(k_1)P(k_2)\times\Big[\bar{b}_{\alpha,1}T_2(\mathbf{k}_1,\mathbf{k}_2|\mathbf{k}_3) + f(\Omega)T_3(\mathbf{k}_1,\mathbf{k}_2|\mathbf{k}_3) + \frac{\bar{b}_{\alpha,2}}{2} + \bar{b}_{\alpha,0}T_4(\mathbf{k}_1,\mathbf{k}_2|\mathbf{k}_3)\Big]\Big\} + 2\,\mathrm{cyc}; \tag{46}$$

this is equivalent to that found by [35,37]. We also defined the 1- and 2-halo *"effective"* number densities to be

$$\frac{1}{\bar{n}^2_{\alpha,1\mathrm{H}}} = \frac{\langle W_\alpha^3\rangle}{\langle W_\alpha\rangle^3}; \tag{47}$$

$$\frac{1}{\bar{n}_{\alpha,2\mathrm{H}}} = \frac{\langle b_1(M)[W_\alpha]^2\rangle}{\langle W_\alpha\rangle^2}\bar{b}_{\alpha,1} + \frac{f(\Omega)^2}{5}\frac{\langle[W_\alpha]^2\rangle}{\langle W_\alpha\rangle^3} + \frac{f(\Omega)}{3}\times\left[\frac{\langle[W_\alpha]^2\rangle}{\langle W_\alpha\rangle^2}\bar{b}_{\alpha,1} + \frac{\langle b_1(M)[W_\alpha]^2\rangle}{\langle W_\alpha\rangle^3}\right]. \tag{48}$$

Our final expression for the large-scale limit (Eq. (45)) is similar to the standard theoretical expectation for the bispectrum recovered from a Poisson point process sampling of a continuous field (cf. Section 43 in [73]). However, the halo model effective shot-noise terms (the last two terms on the right-hand side of Eq. (45)), are very different from the standard form, which would simply have e.g.

$\bar{n}_{\alpha,2\mathrm{H}} = \bar{n}_\alpha$. These effective number densities, Eqs. (47) and (48), represent the fact that in the halo model we assume that dark matter haloes are Poisson sampled into the density field and that the tracer particles are injected into these haloes, and so simply act as different weights. The issue of sampling tracer particles into the density field has some important implications for how one should extract information from galaxy surveys. We shall reserve this investigation for future work.

In Appendix F we present a short discussion of how these shot-noise corrections can impact the reduced bispectrum. The main results are as follows: For standard shot noise, and in the low-sampling limit there is no configuration dependence and $Q^{\mathrm{d}} = 1/3$, subscript d denotes discrete. For the case where shot noise is subdominant, the Q^{d} is reduced relative to the continuum limit Q for all configurations. In the halo model, and in the low-sampling limit, again there is no configuration dependence and $Q^{\mathrm{HM}} = \langle [W_\alpha]^3 \rangle \langle [W_\alpha] \rangle / 3 \langle [W_\alpha]^2 \rangle^2$. For the case of subdominant shot noise, Q^{HM} is not necessarily smaller than the continuum limit case. In Sec. VI we show some tentative evidence for these effects in the measurements from our numerical simulations.

Before continuing, it should also be noted that on setting $f(\Omega) = 0$, one may recover the 1-loop PT bispectrum in real space for a set of biased tracer particles α.

D. The small-scale limit and hierarchical models

On small scales, the bispectrum is dominated by the 1-halo term, given by Eq. (32). Our understanding of its behavior in this limit can be guided by considering the case where all haloes are of the same mass. In this situation we have $n(M) \to \delta^D(M - M')\bar{n}_{\mathrm{H}}$ and $\bar{\rho}_\alpha \to \bar{n}_{\mathrm{H}}[W_\alpha]$. Applying these conditions to Eq. (32), we have

$$\bar{B}^{\,s}_{1\mathrm{H}}(k_1, k_2, \theta_{12}|M) = \frac{1}{4\pi \bar{n}_{\mathrm{H}}^2} \int d\gamma_1 d(\cos\gamma_2) \times \prod_{i=1}^{3} \{U(k_i|M)\mathcal{V}(\mu_i k_i|M)\}. \quad (49)$$

We may follow this same procedure for the power spectrum (see Eq. (E2)) and so construct the reduced bispectrum, whence

$$\bar{Q}_s = \frac{\int d\gamma_1 d(\cos\gamma_2) \prod_{i=1}^{3} \{\mathcal{V}(\mu_i k_i|M)/U(k_i|M)\}/4\pi}{\mathcal{R}^{(0)}_{1,2}(a_1)\mathcal{R}^{(0)}_{1,2}(a_2)/U(k_3|M)^2 + 2\,\mathrm{cyc}}, \quad (50)$$

where $\mathcal{R}^{(0)}_{1,2}(a_1)$ is given by Eq. (E9). Notice that this expression no longer depends on the weights $[W_\alpha]$ or number densities of tracers $\bar{n}_{\mathrm{H}}$, but simply the real-space profile and the 1-PT velocity profile. If the density and velocity profiles were mass independent, then Eq. (50) would predict the same configuration dependence for all haloes. However, for realistic redshift-space profiles, this is not the case (see Appendix B). Thus, if the halo model is a good description for small-scale clustering, then the hierarchical model is unlikely to be correct in real or redshift space, and we may generally extend this statement to any tracers of the density field. Finally, and somewhat interestingly, notice that if the ratio $\mathcal{V}(\mu_i k_i|M)/U(k_i|M)$ is mass independent, then the configuration dependence of the bispectrum becomes universal, modulo an amplitude offset.

E. The White-Seljak approximation

The White-Seljak approximation (hereafter WS) is the supposition that haloes are randomly oriented relative to each other so that in computing the monopole of the bispectrum, orientation averages can be taken separately over each individual halo and over the large-scale orientation of the halo relative to each other [45,46]. In the triaxial halo model, [70] showed that the overall contribution from halo alignment to the matter power spectrum was negligible. Thus we may similarly assume that on large scales the 2- and 3-halo terms will not be sensitive to the orientation of the FOGs—and this allows us to use the isotropic redshift-space density profiles instead of the anisotropic profiles. However, since the bispectrum is more sensitive than the power spectrum to the shapes of structure, we shall be a little more cautious, and demonstrate the validity of this approximation in Sec. V A.

In the WS approximation we therefore take

$$\bar{\psi}^{(i)}_{\delta,1}(k_1) \equiv \frac{1}{4\pi} \int d\gamma_1 d(\cos\gamma_2) \psi^{(i)}_{\delta,1}(\mathbf{k}'_1),$$
$$\bar{\psi}^{(i)}_{\delta,2}(k_1, k_2, \theta_{12}) \equiv \frac{1}{4\pi} \int d\gamma_1 d(\cos\gamma_2) \psi^{(i)}_{\delta,2}(\mathbf{k}'_1, \mathbf{k}'_2), \quad (51)$$

and with similar expressions for the $\bar{\psi}_{v,j}$ functions. On replacement of these terms into Eq. (37) we find that the 2-halo term simplifies to

$$\begin{aligned}\bar{B}^{\,s,\mathrm{WS}}_{\alpha,2\mathrm{H}}(k_1, k_2, \theta_{12}) = P(k_2)\{&\bar{\psi}^{(1)}_{\delta,2}(k_1, k_3, \theta_{13})\bar{\psi}^{(1)}_{\delta,1}(k_2) \\ &+ \tfrac{1}{3}[\bar{\psi}_{v,2}(k_1, k_3, \theta_{13})\bar{\psi}^{(1)}_{\delta,1}(k_2) \\ &+ \bar{\psi}^{(1)}_{\delta,2}(k_1, k_3, \theta_{13})\bar{\psi}_{v,1}(k_2)] \\ &+ \tfrac{1}{5}\bar{\psi}_{v,2}(k_1, k_3, \theta_{13})\bar{\psi}_{v,1}(k_2)\} + 2\,\mathrm{cyc}.\end{aligned} \quad (52)$$

Similarly, on applying the WS approximation to Eq. (38), the 3-halo term reduces to

$$\bar{B}^{s,\mathrm{WS}}_{\alpha,3\mathrm{H}}(k_1,k_2,\theta_{12}) = 2P(k_1)P(k_2)\int\frac{d\gamma_1}{4\pi}d(\cos\gamma_2)\bar{T}_1(\mathbf{k}_1',\mathbf{k}_2')\Big[T_2(\mathbf{k}_1',\mathbf{k}_2'|\mathbf{k}_3')\bar{\psi}^{(1)}_{\delta,1}(k_3) + T_3(\mathbf{k}_1',\mathbf{k}_2'|\mathbf{k}_3')\bar{\psi}_{v,1}(k_3) + \mathcal{W}_{12,3}\frac{\bar{\psi}^{(2)}_{\delta,1}(k_3)}{2} + T_4(\mathbf{k}_1',\mathbf{k}_2'|\mathbf{k}_3')\bar{\psi}^{(0)}_{\delta,1}(k_3)\Big] + 2\,\mathrm{cyc}; \quad (53)$$

where

$$\bar{T}_1(\mathbf{k}_i,\mathbf{k}_j) = \prod_{m=i,j}\{\bar{\psi}^{(1)}_{\delta,1}(k_m) + \mu_m^2[\bar{\psi}_{v,1}(k_m) + f(\Omega)\bar{\psi}^{(0)}_{\delta,1}(k_m)]\}. \quad (54)$$

This completes our analytic investigation. In the next sections we shall provide numerical evaluation of our expressions for the bispectrum.

V. ANALYTIC RESULTS

A. Testing the WS approximation

Figure 1 compares the predictions for the reduced redshift-space matter bispectrum (Eqs. (32), (37), and (38)) with the WS approximate expressions Eqs. (32), (52), and (53). The four panels show k-space triangles with $k_2/k_1 = 2$ and with $k_1 = \{0.05, 0.1, 0.5, 1.0\}h$ Mpc^{-1}.

On very large scales (top left panel), $k = 0.05h$ Mpc^{-1}, the predictions are dominated by the 3-halo term, and the approximate expressions (thin blue lines) are in almost perfect agreement with the exact halo model predictions (thick red lines), with $<2\%$ deviations across different configurations. This is to be expected following our derivation of the bispectrum in the large-scale limit, cf. Eq. (45); i.e., there is no dependence on the halo profiles and so the WS approximation does not play a role here. On slightly smaller scales (top right panel) $k_1 = 0.1h$ Mpc^{-1}, small but significant departures are found at the level of $<10\%$. It can be seen that these are entirely due to deviations in the 3-halo term—the order in which we spherically average the profiles is now important. However, on still smaller scales (bottom left panel) $k_1 = 0.1h$ Mpc^{-1}, while the discrepancy between the approximate and exact 3-halo term becomes larger, the 1- and 2-halo terms begin to dominate and so the difference in the total appears $<6\%$. Finally, on the smallest scales considered, the 1-halo term comes to fully dominate and since no approximation is made here the results are in good agreement, $<5\%$.

For a given scale, the largest deviations typically appear for the case of colinear triangles, i.e. where all three k-vectors are colinear. This leads us to suppose that the equilateral bispectrum as a function of scale will show agreement at the level of $<5\%$ across a wide range of scales under this approximation. Since current observational measurements of the bispectrum on large scales have sample and cosmic variance errors of the order $\sim 50\%$ on scales $k_1 \sim 0.1h$ Mpc^{-1}, going down to several percent at $k_1 \sim 1h$ Mpc^{-1}, we anticipate that, at least for current data, the WS approximation should be useful. We highlight again that the main advantage of this approximation is the increased speed with which one can compute the bispectrum: the $\psi^{(i)}_{\delta,j}$ and $\psi_{v,j}$ functions are only evaluated once for a particular configuration, as opposed to thousands of times. However, in all that follows we shall only show results for the exact evaluation (no WS approximation) of our redshift-space halo model.

B. Comparison with perturbation theory

Figure 2 compares the analytic predictions for the reduced bispectrum from our model with corresponding results from PT. The four panels show again k-space triangles with $k_2/k_1 = 2$ and for the same scales as presented in Fig. 1. The solid (red) lines in each panel show our HMs predictions (recall HMs means halo model in redshift space) in the WS approximation. The (red) dash lines show the PTs predictions, as given by our Eq. (46). The (blue) dotted lines correspond to real-space PT predictions.

On the largest scales $k_1 = 0.05h$ Mpc^{-1} (top left panel), the HMs and PT results match almost perfectly: the configuration dependence shows excess signal for colinear triangles, indicating that on these very large scales nonlinearity induces structures that are, on average, more filamentary than spherical [35,74] (in this diagram spherical perturbations are best probed by isosceles triangles, $\theta_{12} \sim 2\pi/3$). However, we notice that there is a small deviation $<5\%$ for the situation where the k_1 and k_2 vectors are aligned. This owes to the fact that the 1- and 2-halo terms are nonvanishing as $k \to 0$, and as discussed in Sec. IV C, this gives rise to an "effective shot-noise"-like behavior. A discussion of why colinear $k_1 - k_2$ triangles (i.e. $\theta_{12} = 0$) are more preferentially affected is given in Appendix F). It should also be noted that unlike for the case of standard shot noise, $Q^{\mathrm{HM}} > Q^{\mathrm{PT}}$ for configurations close to isosceles triangles.

On slightly smaller scales $k_1 = 0.1h$ Mpc^{-1}, both the PT and PTs predictions show a small increase in configuration dependence, with the PTs having slightly more signal for colinear triangles than PT. The HMs predictions are in qualitative agreement with PT. However, the flattening off seen in the previous panel is now much more apparent. Recalling the corresponding panel in Fig. 1, it can be seen that this is attributed to the rapidly rising 1- and 2-halo terms.

On smaller scales still $k_1 = 0.5h$ Mpc^{-1}, the PT and PTs predictions continue their previous trends, exhibiting a slightly increased configuration dependence. However, the

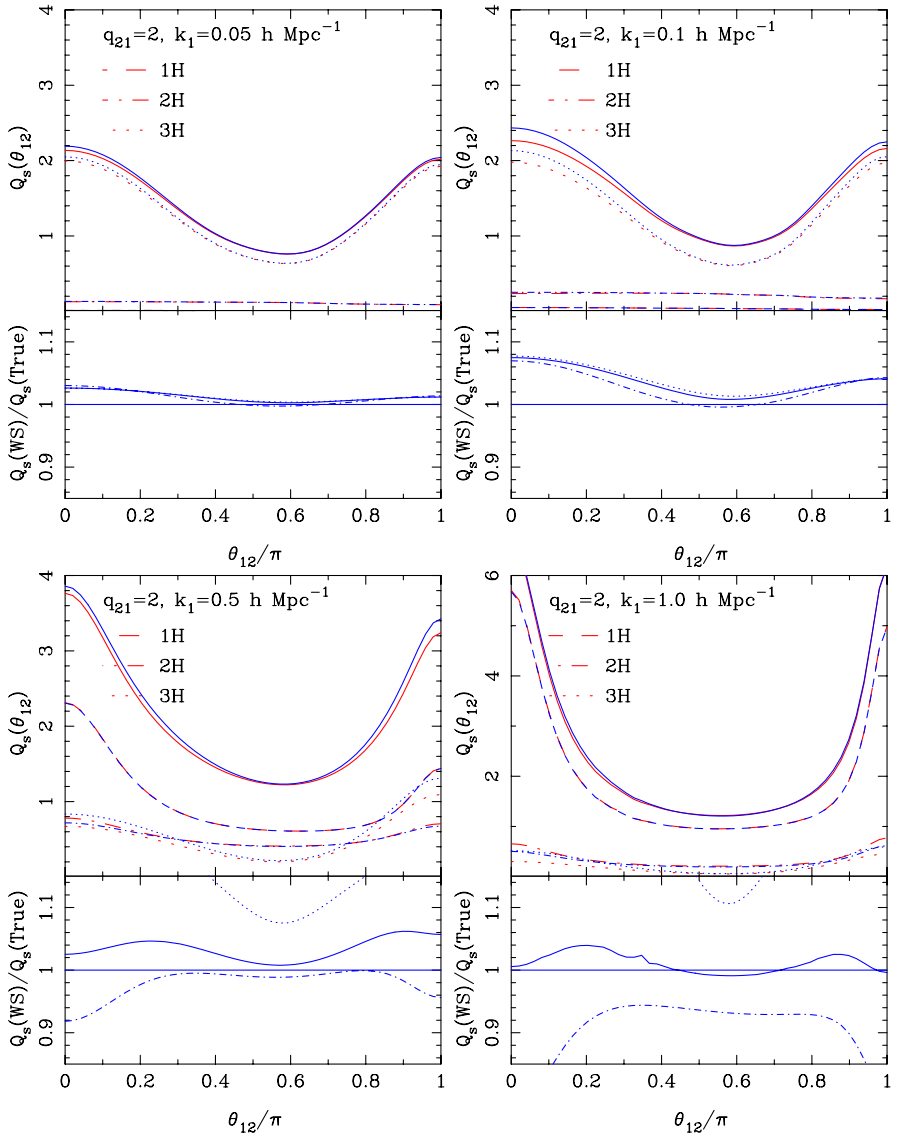

FIG. 1 (color online). Configuration dependence of the reduced bispectrum monopole in redshift space—comparison of the predictions from the exact halo model expressions with those under the WS approximation. Top sections of each panel show results for triangles with $k_2/k_1 = 2$ and on scales: $k_1 = \{0.05, 0.1, 0.5, 1.0\}h$ Mpc^{-1}. The dash, dot-dash, and dotted lines in each panel correspond to the 1-, 2-, and 3-halo terms, respectively. The solid lines correspond to the sum. Thick (red) and thin (blue) lines are the exact halo model and WS approximate results, respectively. Bottom sections of each panel show the ratio of the total WS approximate bispectra to the exact halo model calculation. Line styles have the same meaning as in the top panels.

HMs predictions are quite different, having a very strong U-shaped configuration dependence. This owes to the 1- and 2-halo terms becoming dominant.

On the smallest scales considered $k_1 = 1.0h$ Mpc^{-1}, the HMs predictions show a dramatic configuration dependence, with a very strong signal for colinear triangles and a broad plateau for triangle shapes around isosceles configurations—this is the "U-shape," which was first noted in the bispectrum by [35] and in the 3-point correlation function by [36]. Recalling Fig. 1 (bottom left panel), we see here that the prediction is completely dominated by the 1-halo term, and so this U-shape feature is simply an imprint of the halo shape in redshift space—the FOG. This result constitutes a more direct demonstration of the discussion from Sec. IV D, that hierarchical models are unlikely to be a good description for the higher-order clustering statistics.

In this section we have shown from purely theoretical considerations that to use the galaxy bispectrum on large scales $k_1 < 0.1h$ Mpc^{-1} as a precise tool for cosmology, one needs to understand exactly how to include the FOG effect into the modeling and also how to include nontrivial discreteness effects of matter. In the next section we confront the model with results from numerical simulations.

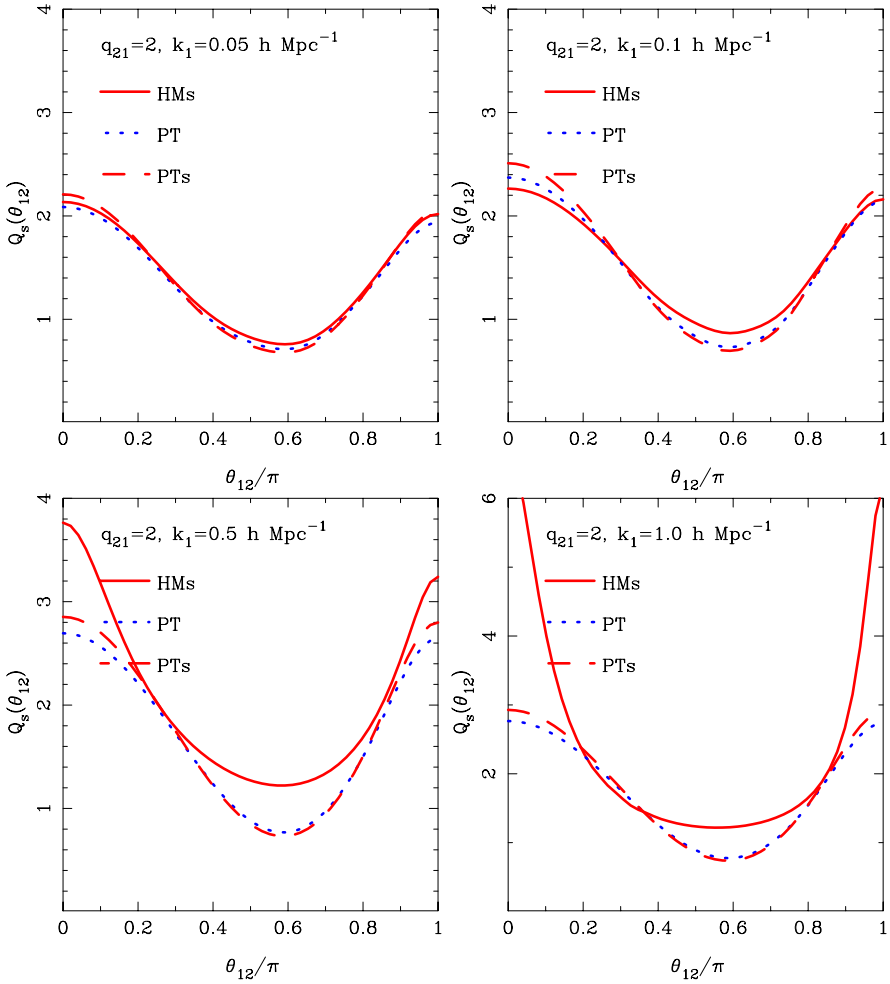

FIG. 2 (color online). Comparison of analytic model predictions with results from PT. The configuration dependence is shown for triangles with $k_2/k_1 = 2$ and on scales: $k_1 = \{0.05, 0.1, 0.5, 1.0\}h$ Mpc^{-1}. In all panels: solid (red) lines represent redshift-space halo model predictions (HMs); dash (red) lines correspond to redshift-space tree-level PT (PTs) [35]; and dotted (blue) lines correspond to real-space tree-level PT.

VI. COMPARISON WITH NUMERICAL SIMULATIONS

A. Numerical simulations

In order to test our redshift-space bispectrum we generated an ensemble of 8 LCDM simulations, these were identical in every way, except that for each simulation different random realizations of the initial Fourier modes were drawn. The cosmological parameters for the ensemble were selected to be in broad agreement with the WMAP best-fit model [5]: $\Omega_m = 0.27$, $\Omega_\Lambda = 0.73$, $\Omega_b = 0.046$, $h = 0.72$, and $\sigma_8(z = 0) = 0.9$. We used the `cmbfast` [57] code to generate the linear theory transfer function, and we adopted the standard parameter choices, and took the transfer function output redshift to be at $z = 0$. The initial conditions for each simulation were then laid down at $z = 49$ using the publicly available `2LPT` initial conditions generator [75,76]. Subsequent gravitational evolution of the equations of motion was then performed using the publicly available `Gadget2` code [77]. Each simulation was run with $N = 400^3$ particles in a comoving volume of length $L = 512^3 h^{-1}$ Mpc and with a comoving force softening set to $70h$ kpc. The simulations were performed using a 4-way dual core Opteron processor system, and each ran to completion in roughly $\sim$1800 time steps from redshift $z = 49$ to $z = 0$ and this translates to $\sim$2 days of wall clock time.

B. Estimating the power spectrum

Before comparing our analytic model with the bispectra estimates from the simulations, it is instructive to compute the real and redshift-space power spectra of the $z = 0$ outputs of the ensemble.

The density Fourier modes are estimated using the conventional fast fourier transform (FFT) method: the dark matter particles were assigned to a regular cubical grid using the "Cloud-In-Cell" (CIC) scheme [78]. The FFT of the gridded density field was then computed using the

publicly available FFTW routines [79]. Each resulting Fourier mode was then corrected for the convolution with the mesh by dividing out the Fourier transform of the mass-assignment window function. For the CIC algorithm this corresponds to the following operation:

$$\delta_{\rm d}(\mathbf{k}) = \delta_{\rm g}(\mathbf{k})/W_{\rm CIC}(\mathbf{k}), \tag{55}$$

where

$$W_{\rm CIC}(\mathbf{k}) = \prod_{i=1,3}\left\{\left[\frac{\sin[\pi k_i/2k_{\rm Ny}]}{[\pi k_i/2k_{\rm Ny}]}\right]^2\right\}, \tag{56}$$

where subscript d and g denote discrete and grid quantities, and where $k_{\rm Ny} = \pi N_{\rm g}/L$ is the Nyquist frequency of the mesh and $N_{\rm g}$ is the number of grid cells.

The power spectra of the discrete particles on scale k_l are then estimated by performing the following sums:

$$\hat{\bar{P}}_{\rm d}(k_l) = \frac{V_\mu}{M}\sum_{l=1}^{M}|\delta_{\rm d}(\mathbf{k}_l)|^2, \tag{57}$$

where M is the number of Fourier modes in a spherical shell in k-space of thickness Δk. Note that the mode-by-mode correction differs from the analysis of [54,80] where the correction for charge assignment was performed by computing the spherically averaged window and dividing it out. Mode-by-mode correction for the power spectrum was also performed in [38,74].

Figure 3 shows the mean and 1-σ errors for the power spectra of dark matter particles in both real and redshift space. The errors are computed directly from the 8 realizations. The spectra were computed using a 1024^3 FFT and we show all frequencies up to the Nyquist frequency—the highest k-modes show signs of increased power from both Poison shot noise (triple dot-dash green line) and the aliasing of power from smaller scales. We note that on the largest scales probed, the power spectra show a sequence of wiggles, these are the well-known baryonic acoustic oscillations (BAO) that have been discussed much in recent times [3,38,81–83]—we shall not discuss these in this paper. The solid lines show the total halo model predictions in real (blue, darker lines) and redshift space (red, lighter lines). We see that, while the real-space model does reasonably well, with an accuracy of the order ~10%, the redshift-space predictions fare less well, especially for scales $k > 0.2h$ Mpc^{-1}. Here the model systematically underpredicts the data by roughly ~20%.

These predictions were very sensitive to how we modeled the FOG effects, i.e. the 1D velocity dispersion of particles within haloes $\nu(k|M)$. Originally, we had simply used Eq. (B12) with $\epsilon = 1$, however in this case the predictions were particularly poor. We therefore investigated the $M - \sigma_{\rm 1D}$ relation in our simulations more closely. Using a standard friends-of-friends (FoF) algorithm with link length $f = 0.2$, we located all haloes with $M > 1.0 \times 10^{13} M_\odot/h$. The 1D velocity dispersions

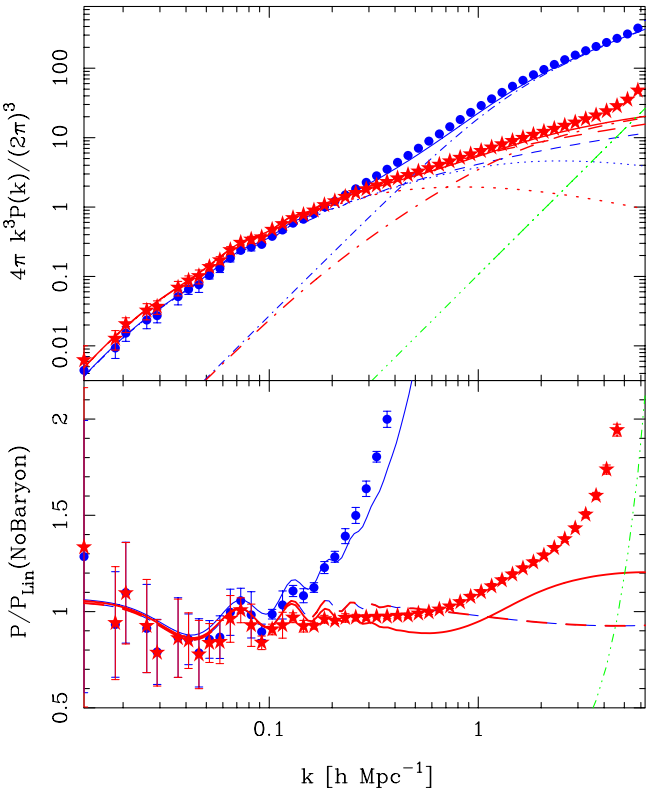

FIG. 3 (color online). Real and redshift-space power spectrum of dark matter particles at $z = 0$ measured from the ensemble of LCDM simulations. Top panel: The power spectrum. Blue (darker) and red (lighter) points show real and redshift-space quantities, respectively. The solid, dot-dash, and dotted lines show the total halo model, 1-halo, and 2-halo terms. The triple dot-dash curve shows the predictions for the Poisson shot-noise error. The dash line shows the linear theory. Bottom panel: The measured power spectra ratioed with a no-baryon linear theory power spectrum that has the same overall transfer function shape. Note that for the redshift-space spectra, we have scaled out the Kaiser boost.

were then estimated for each halo and binned as a function of mass. We found that $\epsilon = 1$ overpredicted the measured values by >20%. Fitting on ϵ it was found that $\epsilon = 0.76$ provided a better fit to the data, but it was not perfect, it having an accuracy no better than ~10% (see Fig. 6). As can be seen from the figure using $\epsilon = 0.76$ does not generate the correct power spectrum.

A possible reason for this discrepancy could be that the 2-halo term in the redshift-space power spectrum only includes linear halo motions—nonlinear terms do contribute to this term (see [42,44,83]) and inclusion of these nonlinear corrections may help alleviate this problem. Another is that the concentration—mass relation, which is vital for getting the correct normalization of the halo density profiles, may not be sufficiently accurate. Indeed we note a small discrepancy between the real-space measurements and halo model predictions. Recent improvements on this relation by [84] may help to alleviate this

problem. Also, we have neglected the scatter in the concentration parameter, and it is well known that this can change the predictions by a few tens of percent in the nonlinear regime [85]. Additionally, there is the issue of halo triaxiality [20,70]. A further possibility is the breakdown of our model for the halo phase-space distribution: as noted by [86,87], while the isotropic model for velocities appears reasonable in the outer regions of haloes, especially for low to intermediate masses, there are small departures in the inner regions. Reference [87] also shows that the 3D velocity dispersion declines as a function of radius by $\sim 25\%$, out to the virial radius. We shall not pursue these subtle corrections here, since our purpose is simply to present the theoretical framework and show that it, nevertheless, gives reasonable agreement with the simulation data. It should also be understood that these more complex descriptions can be incorporated into our calculational framework.

C. Estimating the bispectrum

Our estimator for the bin and spherical averaged bispectrum was developed following the work of [74], but with some changes. Our estimator can be written:

$$\hat{\bar{B}}_{\rm d}(k_1, k_2, \theta_{12}) = \frac{1}{V_1 V_2} \int_{V_1,V_2} \frac{d^3q_1}{(2\pi)^3} \frac{d^3q_2}{(2\pi)^3} \times \hat{B}_{\rm d}(\mathbf{q}_1, \mathbf{q}_2, -\mathbf{q}_1 - \mathbf{q}_2), \quad (58)$$

where

$$V_i = \int_{k_i-\Delta k/2}^{k_i+\Delta k/2} \frac{d^3q}{(2\pi)^3} = \frac{4\pi k_i^2 \Delta k}{(2\pi)^3}\left[1 + \frac{(\Delta k)^2}{12 k_i^2}\right]. \quad (59)$$

A practical implementation of this estimator involves computing the following sum:

$$\hat{\bar{B}}_{\rm d} = \frac{V_\mu^2}{N_{\rm tri}} \sum_{\mathbf{n}_1,\mathbf{n}_2}^{N_{\rm tri}} \mathcal{R}e[\delta_{\rm d}(\mathbf{k}_{\mathbf{n}_1})\delta_{\rm d}(\mathbf{k}_{\mathbf{n}_2})\delta_{\rm d}(\mathbf{k}_{-\mathbf{n}_1-\mathbf{n}_2})], \quad (60)$$

where $\mathbf{n}_i$ is an integer vector from the k-space origin to a mesh point and so labels the modes, and where $N_{\rm tri}$ represents the number of independent momentum conserving k-vector triangles in the shells V_1 and V_2. In the above we take only the real part of the product of the three Fourier modes, owing to the reality of the bispectrum (see Eq. (A21)). Note that when computing the sums over k-space triangles we randomly sample modes from the set of all possible triangles. Typically we limit the computations to 10^4 modes per shell (i.e. 10^8 triangles). This method gives a sufficient number of independent k-space triangles for a high accuracy estimate, while keeping code execution times tolerable.

To accurately estimate Q we are also required to estimate the combination $\bar{Q}_{\rm fac} \equiv \bar{P}(k_1)\bar{P}(k_2) + \bar{P}(k_2)\bar{P}(k_3) + \bar{P}(k_3)\bar{P}(k_1)$. There are several approaches to achieving this: one, we could simply estimate the power spectrum as in Eq. (57) and then construct $\bar{Q}_{\rm fac}$ from this; alternatively one can compute an estimate of $\bar{Q}_{\rm fac}$ using only those same modes that are used to estimate $\bar{B}$. We adopt this latter approach since we expect that it will reduce sample variance. Along with our estimates for B, we also therefore accumulate

$$\hat{\bar{P}}_{i,{\rm d}} = \frac{V_\mu}{N_{\rm tri}} \sum_{\mathbf{n}_i}^{N_{\rm tri}} |\delta_{\rm d}(\mathbf{k}_{\mathbf{n}_i})|^2; \qquad i \in \{1, 2\}; \quad (61)$$

$$\hat{\bar{P}}_{3,{\rm d}}(\theta_{12}) = \frac{V_\mu}{N_{\rm tri}} \sum_{\mathbf{n}_3}^{N_{\rm tri}} |\delta_{\rm d}(\mathbf{k}_{\mathbf{n}_3}[\theta_{12}])|^2; \quad (62)$$

$$\hat{\bar{Q}}_{\rm fac,d}(\theta_{12}) \equiv \hat{\bar{P}}_{1,{\rm d}}\hat{\bar{P}}_{2,{\rm d}} + \hat{\bar{P}}_{2,{\rm d}}\hat{\bar{P}}_{3,{\rm d}} + \hat{\bar{P}}_{3,{\rm d}}\hat{\bar{P}}_{1,{\rm d}}. \quad (63)$$

We draw close attention to the fact that these estimates for the power spectra $\hat{\bar{P}}_1$, $\hat{\bar{P}}_2$, and $\hat{\bar{P}}_3$ are not the same as in Eq. (57): in the above case we average over all k-space triangles that are used and not just the unique modes. We have also made it explicitly clear that the estimates for $\hat{\bar{P}}_1$ and $\hat{\bar{P}}_2$ do not change with θ_{12}, but that $\hat{\bar{P}}_3$ does. Following this procedure helps to reduce cosmic variance. We also note the following pitfall: had we estimated $Q_{\rm fac}$ for each k-space triangle and then averaged these estimates over all triangles, i.e. taken $\bar{Q}_{\rm fac} \equiv \overline{P(k_1)P(k_2)} + 2\,{\rm cyc}$, then we would have been angle averaging products of power spectra. In real space, where P is an isotropic function on the sphere, this makes no difference, however in redshift space, where P is anisotropic, this approach would be incorrect and no U-shape would be seen in Q.

In order to correct B and P for discreteness we also estimate the shot-noise terms as [73]:

$$\hat{\bar{P}}_{\rm shot} \equiv \frac{V_\mu}{N}; \quad (64)$$

$$\hat{\bar{B}}_{\rm shot} \equiv \frac{V_\mu}{N}[\hat{\bar{P}}_{1,{\rm d}} + \hat{\bar{P}}_{2,{\rm d}} + \hat{\bar{P}}_{3,{\rm d}}] + \frac{V_\mu^2}{N^2}; \quad (65)$$

$$\hat{\bar{Q}}_{\rm fac,shot} \equiv 2\frac{V_\mu}{N}[\hat{\bar{P}}_{1,{\rm d}} + \hat{\bar{P}}_{2,{\rm d}} + \hat{\bar{P}}_{3,{\rm d}}] + 3\frac{V_\mu^2}{N^2}. \quad (66)$$

Estimates of the shot-noise corrected continuous spectra are then arrived at through the following set of operations:

$$\hat{\bar{P}} = \hat{\bar{P}}_{\rm d} - \hat{\bar{P}}_{\rm shot}; \quad (67)$$

$$\hat{\bar{B}} = \hat{\bar{B}}_{\rm d} - \hat{\bar{B}}_{\rm shot}; \quad (68)$$

$$\hat{\bar{Q}}_{\rm fac} = \hat{\bar{Q}}_{\rm fac,d} - \hat{\bar{Q}}_{\rm fac,shot}; \quad (69)$$

$$\hat{\bar{Q}} = \hat{\bar{B}}/\hat{\bar{Q}}_{\rm fac}. \quad (70)$$

In our measurements we shall show both spectra with and without the shot-noise corrections.

Lastly, as a consistency check, we also estimate the imaginary bispectrum, which is given by Eq. (60) only now we take the imaginary piece of the product. Thus, if our estimate is correct, then this quantity should on average be zero. However, as the number of independent triangles

becomes small the imaginary piece may become nonzero due to statistical fluctuations.

D. Bispectrum results

Figure 4 shows the mean and the 1-σ errors on the mean (i.e. we divide the standard error bars by $1/\sqrt{7}$) for the configuration dependence of the bispectrum $B(k_1, k_2, \theta_{12})$ in both real and redshift space for the 8 LCDM simulations. The four panels show results for k-space triangles with $k_2/k_1 = 2$ and $k_1 = \{0.05, 0.1, 0.5, 1.0\}h$ Mpc^{-1} and thin (blue) and thick (red) lines distinguish between real and redshift-space quantities.

Considering the largest scales ($k = 0.05h$ Mpc^{-1}), we see that the ensemble estimate is rather noisy, this owes to the large sample variance on these scales. Nevertheless, it can be discerned that the redshift-space (large solid stars) estimate has a slightly higher amplitude than the real-space (solid points) estimate. We also note that there are a few bins that give a significant nonzero contribution to the imaginary bispectra. We attribute this to the large sample variance errors, but in the main these points are below the true signal. In all cases the results for the bispectra appear to be consistent with the PT and HM predictions, to within the errors. To say anything more definite on these scales will require much larger simulation volumes, and we shall defer this question for future study.

On intermediate scales ($k = 0.1h$ Mpc^{-1}), the estimates for the real and redshift-space spectra are much more significant, the errors being well defined. This is supported by the fact that the imaginary spectra have amplitudes that are now too small to be plotted. It can be seen that the results have a strong dependence as a function of triangle configuration. On comparing with the PT and PTs, we see that on these scales PT underpredicts the measured quantity by roughly $\sim$20%, whereas PTs overpredicts the amplitude by a similar amount. Considering the predictions of the HM and HMs, it is clear that in real space the model is a significant improvement over PT; whereas in redshift space, while the configuration dependence appears to have been slightly improved, the amplitude is still too large.

On smaller scales ($k = 0.5h$ Mpc^{-1}), we see that the estimates of the spectra are of even higher signal to noise and that they form tight-loci across the configuration. Again the imaginary bispectra are insignificant. It may be noticed that there is a large difference between the real-space PT and the simulation estimate—almost 2 orders of magnitude, this is due to the fact that $B \sim QP^2$ and the power spectrum is significantly larger than linear. However, this dramatic change in the measured bispectrum is captured relatively well by the HM, which underpredicts the result by only $\sim$20%. Turning to the redshift-space results, we are surprised to see that the PT is of the same amplitude and has somewhat similar configuration dependence as the estimate. This agreement seems coincidental, given the poor agreement in real space. In reality the true dynamics on these scales must already be very nonlinear. Lastly, we draw attention to the fact that our HMs result is in excellent agreement with the simulation data.

Examining scales on the order of the virial radii for clusters ($k = 1.0h$ Mpc^{-1}), we see again that the estimates are of very high significance. Again, the HMs predictions are in excellent agreement. This essentially vindicates our form for the 1-halo term, and means that the configuration dependence is very much governed by the FOG distortions.

E. Reduced bispectrum results

Figure 5 shows similar results as in Fig. 4 but for the configuration dependence of the reduced bispectrum, $Q(k_1, k_2, \theta_{12})$. Again errors are shown on the mean of Q.

On the largest scales probed, ($k = 0.05h$ Mpc^{-1}), the estimates are noisy, but there is evidence for an excess of signal for colinear triangles—meaning that on average structures are more filamentary than spherical on the largest scales [35,74]. Also, the data appear to be scattered about the theoretical predictions, with all models being equally good fits to the data.

Considering intermediate scales ($k = 0.1h$ Mpc^{-1}), the estimates are much more significant and possess well-defined configuration dependencies—both showing an excess of signal for colinear triangles. However, the real-space bispectrum appears to be in excess of the redshift-space quantity. This is in contrast to the PT and PTs predictions which, while they qualitatively capture the overall shape, predict the reverse trend, the results being discrepant by roughly $\sim$20%. This problem is also mirrored in the HM and HMs predictions, but the flatter configuration dependence of the data is better captured by the halo model. As was discussed in Sec. IV C, this flattening can be attributed to the impact of the 1- and 2-halo terms acting as effective shot-noise contributions. The amplitude offsets still require explanation, and we refer to our discussion of Sec. VI B for some possible remedies, but to that list we may now add the need for loop corrections to the tree-level bispectra. As was shown in [74], in real space the 1-loop corrections are significant on these large scales.

On smaller scales ($k = 0.5h$ Mpc^{-1}), we see that, as was noted in Fig. 5, the real-space measurements have increased in amplitude and have become much flatter across the configuration—the HM predictions agree rather well with this result. This implies that the statistic is already in the fully nonlinear regime, since the 1- and 2-halo terms are dominating the signal here. There is very little relation between standard PT to the measurements, as expected. Turning to the redshift-space estimates, it can be seen that the configuration dependence displays a reasonably strong U-shape. The PTs predictions do not describe this shape very well, but are not as discrepant as in real space. However, HMs predictions capture the form of the configuration dependence exceptionally well, but are offset by $\sim$10%–20%.

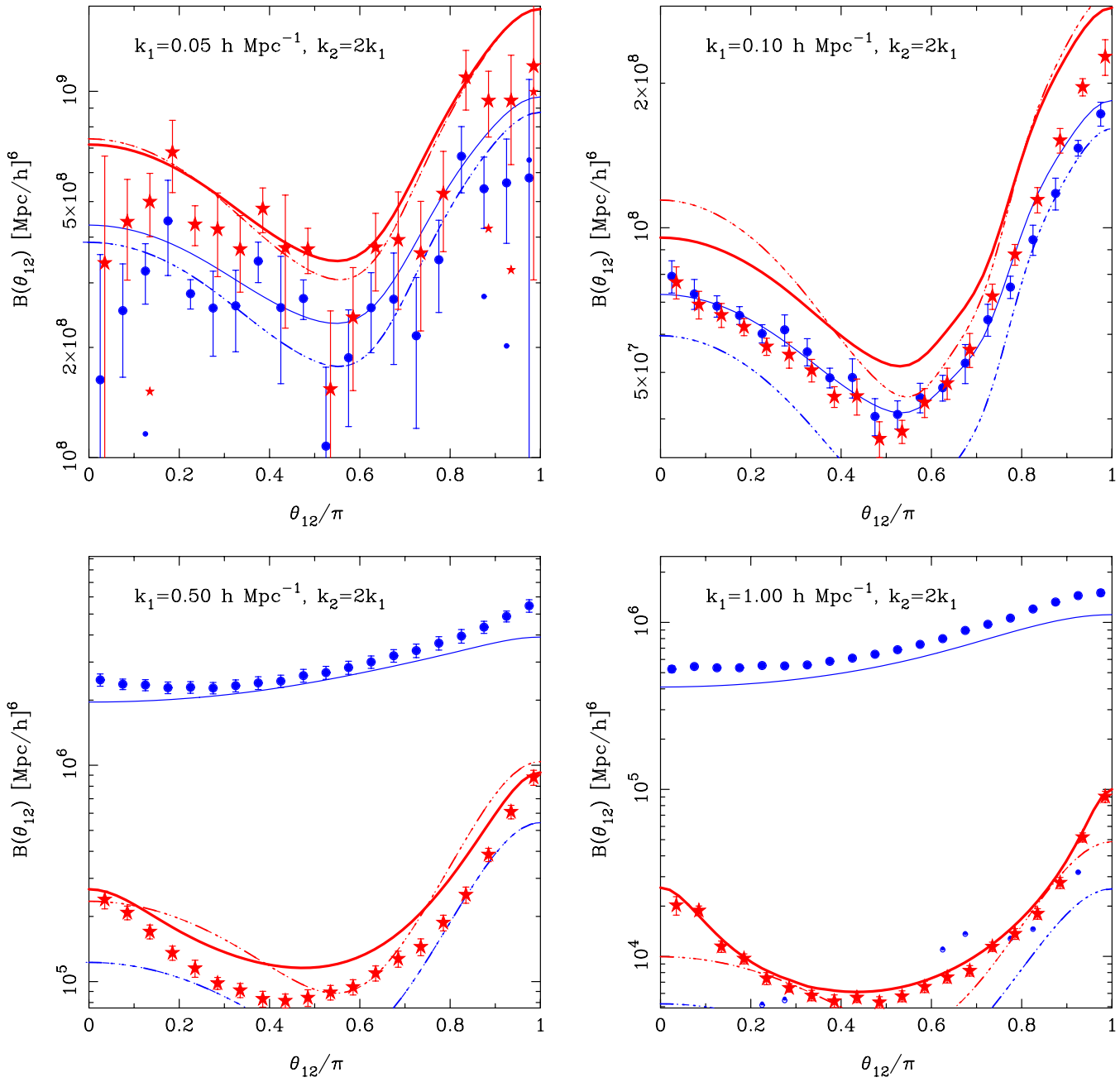

FIG. 4 (color online). Configuration dependence of the bispectrum in real and redshift space measured for the dark matter particles in the ensemble of LCDM simulations. The four panels show the configuration dependence for k-space triangles with $k_2/k_1 = 2$ and for scales $k_1 = \{0.05, 0.1, 0.5, 1.0\}h$ Mpc^{-1}. Red (lighter) and blue (darker) colors distinguish between real and redshift-space quantities. The solid points with error bars show measurements: large solid points are for the real (dots) and redshift-space (stars) monopole bispectra; the corresponding smaller points are the imaginary bispectra (which should be zero). The solid lines show the predictions from HM (thin) and HMs (thick). The triple dot-dash lines show the predictions from PT (thin) and PTs (thick). In the top left panel, for clarity we have suppressed the errors on the imaginary bispectra.

Considering the scales associated with the virial radii of clusters ($k = 1.0h$ Mpc^{-1}), we see that the estimates in real space are surprisingly unchanged and that the HM still provides a very good description of the data. For the redshift-space estimates, we find that there is now a very strong U-shape configuration dependence, in full agreement with the results from [35]. Again, the HMs predictions capture this result remarkably well, although there is a small amplitude offset. It is believed that this may be mitigated by implementing the improvements discussed in Sec. VI B and VI D.

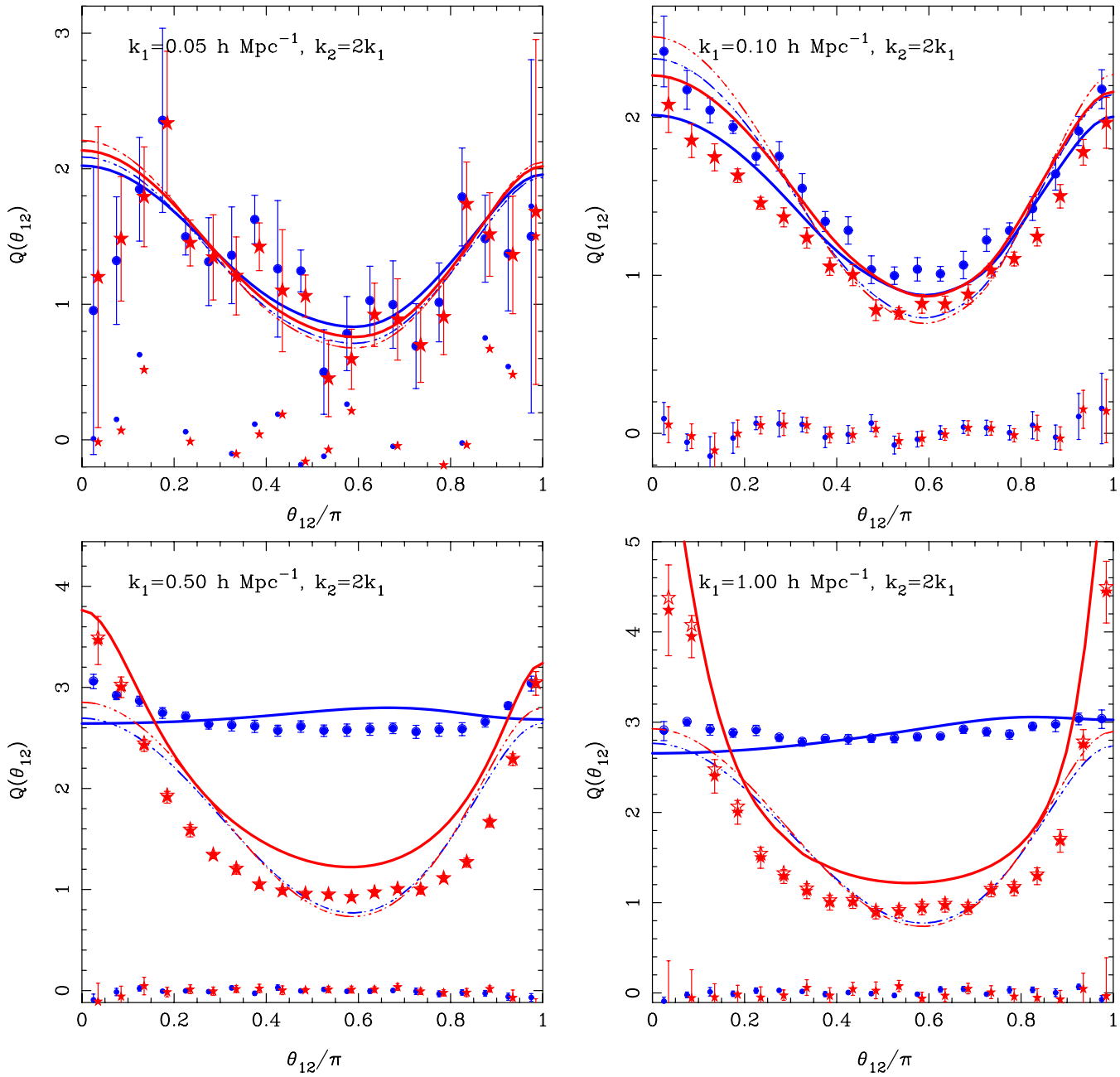

FIG. 5 (color online). Same as Fig. 4 only this time for the reduced bispectrum. Additionally, where visible the open symbols represent the shot-noise corrected estimates.

We also note that the small discrepancies between the real-space HM predictions and the simulations, are entirely consistent with the work of [20]—in reality haloes are triaxial rather than spherical, and this shows up as a characteristic increase in signal for colinear triangles and a suppression for isosceles configurations.

F. Code comparison

Owing to the algorithmic differences between the bispectrum estimation procedure presented in Sec. VI C and that presented in [88], we decided to compare the results obtained from these two approaches. Besides providing an important cross-check, this also enables us to examine how accurately the two codes are recovering Q. Overall we found very good agreement between both methods, and full results are presented in Appendix G.

VII. CONCLUSIONS

In this paper, we have provided a new analytic model for the redshift-space bispectrum of dark matter, haloes, and galaxies in the plane parallel approximation for the redshift-space distortion. On large scales, the model pre-

dictions have a direct correspondence to the nonlinear perturbation theory and on small scales, the predictions are entirely governed by the phase-space density of galaxies/dark matter internal to the haloes. This is the first time that the information from bulk flows and virial motions have been naturally incorporated into an analytic model for the higher-order clustering statistics in redshift space.

In our analytic model, the bispectrum is represented as a sum over three terms; these correspond to all of the possible distinct arrangements of three points in three haloes, and we referred to these as the 1-, 2-, and 3-halo terms. A practical evaluation of the monopole of the bispectrum (a direct observable), with realistic models for halo profiles, abundance, and clustering, required the execution of a set of 4-D numerical integrals. For the terms that involved large-scale correlations (2- and 3-halo terms) it was shown that these expressions could be easily modularized, and so are best computed in parallel. The 1-halo term must be integrated with an efficient higher-dimensional integrator.

It was shown that the large-scale predictions in the model, which are governed by the 2- and 3-halo terms, can be simplified greatly under the approximation that the angle average of the product of anisotropic density profiles and large-scale clustering of halo centers can be performed separately [45,46]. This approximation was accurate to $<10\%$ on scales $k = 0.1h/\mathrm{Mpc}$, elsewhere it was of the order $<5\%$.

The predictions for the bispectrum monopole were compared with analytic PT in real and redshift space. On very large scales $k = 0.05$–$0.1h$ Mpc^{-1}, the model closely agreed with the redshift-space PT predictions, but with some small deviations noticeable. It was argued that these were due to the ''effective'' shot-noise-like behavior of the 1- and 2-halo terms in the low-k limit. On smaller scales $k = 0.5$–$1.0h$ Mpc^{-1} the analytic model showed a dramatic departure from the PT predictions and displayed a U-shaped anisotropy [35,36]. This was the imprint in the configuration dependence of the FOG distortions from nonlinear virial motions. No trace of the PT remained in the model predictions on these scales. The model predictions showed that there was no scale where a hierarchical model provided a good description of the configuration dependence of the bispectrum.

The predictions were then confronted with measurements of the power spectrum, bispectrum, and reduced bispectrum from an ensemble of numerical simulations. On very large scales $k = 0.05h$ Mpc^{-1} it was found that the PT and halo model predictions were equally good, to within the errors. On smaller scales, $k = 0.1h$ Mpc^{-1}, departures between PT and the simulations were noted at the level of $\sim 10\%$–20%. Therefore, studies that use the lowest order PT to extract galaxy bias are unlikely to be robust on scales $k \gtrsim 0.1h/\mathrm{Mpc}$. The halo model was a better description of the data, but was not in perfect agreement. Plausible improvements to the halo model on these scales were discussed. On even smaller scales, $k = 0.5$–$1.0h$ Mpc^{-1}, the configuration dependence of the bispectrum was flat in real space, whereas in redshift space there was a very strong U-shape feature. The numerical results were reasonably well reproduced by our halo model predictions, a significant improvement over PT that breaks down at these scales.

We cross-validated our results from the numerical simulations by comparing our bispectrum estimates with those obtained from an independent code [88]. The results were found to be in very good agreement.

It was also shown that the assumption of isothermal velocities for dark matter in haloes was in error at the level of 10%–20%, as indicated from the 1-D velocity dispersion mass relation for haloes in the simulations. A parameter ϵ was introduced to account for this departure and a best-fit value of $\epsilon = 0.76$ was found. However, this simple change to the model was still unable to reproduce the measured functional form. We thus recognize that to produce robust predictions for galaxy clustering in redshift space at the percent precision level, significant advances in our understanding of the phase-space structure of dark matter in haloes and also of the haloes themselves will be vital for correct interpretation of survey data.

In future work we shall extend our analysis to examine halo and galaxy bispectra. It will also be important to resolve whether or not the halo model's effective shot-noise terms are important for modeling real survey data. Finally, owing to the fact that different galaxy populations are easily and naturally included into our description, it is hoped that this approach will help to facilitate extraction of information from current and future hi-fidelity large-scale structure surveys of the Universe.

ACKNOWLEDGMENTS

The authors thank Uros Seljak, Bhuvnesh Jain, Laura Marian, Cameron McBride, and Bob Nichol for useful discussions. We thank Rob Thacker for advice and encouragement regarding the opteron cluster. We thank Volker Springel for making public his GADGET-2 code. R. E. S. acknowledges support from the Swiss National Foundation. R. E. S. and R. K. S. acknowledge support from the National Science Foundation under Grant No. 0520647. R. S. is partially supported by NSF AST-0607747 and NASA NNG06GH21G.

APPENDIX A: DUALITY OF CLUSTERING STATISTICS

This section defines the configuration and Fourier space clustering statistics and their dual relationship with one another. It also shows how the cosmological assumptions impose certain important conditions upon these statistics.

We shall assume that ensemble averages are taken over a volume, V_μ, of the Universe sufficiently large for the fun-

damental k-space cell volume to be considered infinitesimally small; outside of this large volume our stochastic fields are exactly zero. This allows us to define Fourier transforms in the volume. We shall also let these fields be ergodic, whence ensemble averages are equivalent to averages over volume.

1. Real-space representation: correlation functions

The fractional density field of matter is defined:

$$\delta(\mathbf{x}, t) \equiv [\rho(\mathbf{x}, t) - \bar{\rho}(t)]/\bar{\rho}(t), \tag{A1}$$

where $\rho(\mathbf{x}, t)$ is the local density at coordinates $(\mathbf{x}, t)$ and $\bar{\rho}(t)$ is the density of the homogeneous background at time t. The n-point connected autocorrelation functions of δ represent the excess probability from the product of the individual independent 1-point distributions of obtaining a particular set of values at all points, e.g. the probability of obtaining fluctuations at three points (a, b, c) can be written:

$$P(a, b, c) \equiv P(a)P(b)P(c)[1 + C_2(a, b) + C_2(b, c) + C_2(c, a) + C_3(a, b, c)], \tag{A2}$$

where C_2 and C_3 are the connected 2- and 3-point correlation functions. We may now be clear about what we mean by connected correlation function: the connected correlator may not be reduced to sums over products of lower order connected correlators. In cosmology these are more commonly written:

$$\xi_2(\mathbf{x}_1, \mathbf{x}_2|t) \equiv \langle \delta(\mathbf{x}_1, t)\delta(\mathbf{x}_2, t)\rangle_c; \tag{A3}$$

$$\xi_3(\mathbf{x}_1, \mathbf{x}_2, \mathbf{x}_3|t) \equiv \langle \delta(\mathbf{x}_1, t) \ldots \delta(\mathbf{x}_3, t)\rangle_c; \tag{A4}$$

$$\xi_n(\mathbf{x}_1, \ldots, \mathbf{x}_n|t) \equiv \langle \delta(\mathbf{x}_1, t) \ldots \delta(\mathbf{x}_n, t)\rangle_c. \tag{A5}$$

These functions obey an integral constraint

$$\frac{1}{V_\mu}\int d^3x_n \xi_n(\mathbf{x}_1, \ldots, \mathbf{x}_n) \to 0; \qquad n > 1. \tag{A6}$$

This follows from noting that on marginalizing the probability functions over one variable, say the Nth variable, one finds that the resulting distribution depends on $n-1$-points, and therefore from Eq. (A2) must not depend on the n-point connected correlation function.

If the density field obeys the cosmological principle, that is statistical homogeneity and isotropy on scales greater than the coherence scale of our fields, then the correlation functions are invariant under translation and rotation of the coordinate system. They are also parity invariant real functions and are invariant to exchange of vector arguments. Thus,

$$\xi_n(\mathbf{x}_1, \ldots, \mathbf{x}_n) = \xi_n(\mathbf{x}_1 + \mathbf{x}_0, \ldots, \mathbf{x}_n + \mathbf{x}_0) \quad \text{(translation)}; \tag{A7}$$

$$= \xi_n(\mathcal{R}\mathbf{x}_1, \ldots, \mathcal{R}\mathbf{x}_n) \quad \text{(rotation)}; \tag{A8}$$

$$= \xi_n(-\mathbf{x}_1, \ldots, -\mathbf{x}_n) \quad \text{(parity)}; \tag{A9}$$

$$= \xi_n(\mathbf{x}_2, \mathbf{x}_1, \ldots, \mathbf{x}_n) \quad \text{(exchange)};$$
$$= \xi_n(\mathbf{x}_i, \mathbf{x}_2, \ldots \mathbf{x}_1, \ldots, \mathbf{x}_n). \tag{A10}$$

For anisotropic fields rotation invariance is broken and for inhomogeneous fields translation symmetry is broken. For homogeneous fields we may immediately apply the translational invariance and drop one of the vector arguments in our function. Setting $\mathbf{x}_0 = -\mathbf{x}_n$ in Eq. (A7) gives

$$\xi_n(\mathbf{x}_1, \ldots, \mathbf{x}_n) = \xi_n(\mathbf{x}_{1n}, \ldots, \mathbf{x}_{(n-1)n}), \tag{A11}$$

where $\mathbf{x}_{ij} \equiv \mathbf{x}_i - \mathbf{x}_j$ and we shall not write the zero argument in the nth space. In this paper we will mainly be concerned with clustering statistics that obey homogeneity, but are anisotropic, as this is exactly the case for the redshift-space distortion in the plane parallel approximation. Lastly, we have the closure relation: $\mathbf{x}_{21} + \mathbf{x}_{32} + \cdots + \mathbf{x}_{1n} = \mathbf{0}$.

2. Fourier space representation: poly-spectra

Under the conditions stated earlier, the density field $\delta(\mathbf{x}, t)$ may be equivalently written as an infinite sum over plane waves through the Fourier transform, where our Fourier convention is

$$\delta(\mathbf{x}) = \frac{V_\mu}{(2\pi)^3}\int d^3k \delta(\mathbf{k}) e^{-i\mathbf{k}\cdot\mathbf{x}}$$
$$\Leftrightarrow \delta(\mathbf{k}) = \frac{1}{V_\mu}\int d^3x \delta(\mathbf{x}) e^{i\mathbf{k}\cdot\mathbf{x}}. \tag{A12}$$

Transforming the density terms in Eqs. (A3)–(A5), leads to

$$\xi_2(\mathbf{r}_{12}) = \int \prod_{i=1}^{1}\left\{\frac{d^3k_i}{(2\pi)^3}\right\} P_2(\mathbf{k}_1, \mathbf{k}_2) e^{-i\mathbf{k}_1\cdot\mathbf{r}_{12}}; \quad [\mathbf{k}_1 + \mathbf{k}_2 = \mathbf{0}], \tag{A13}$$

$$\xi_3(\mathbf{r}_{13}, \mathbf{r}_{23}) = \int \prod_{i=1}^{2}\left\{\frac{d^3k_i}{(2\pi)^3}\right\} P_3(\mathbf{k}_1, \mathbf{k}_2, \mathbf{k}_3) e^{-i\mathbf{k}_1\cdot\mathbf{r}_{13} - i\mathbf{k}_2\cdot\mathbf{r}_{23}}; \quad [\mathbf{k}_1 + \mathbf{k}_2 + \mathbf{k}_3 = \mathbf{0}], \tag{A14}$$

$$\xi_n(\mathbf{r}_{1n}, \ldots, \mathbf{r}_{(n-1)n}) = \int \prod_{i=1}^{n-1}\left\{\frac{d^3k_i}{(2\pi)^3}\right\} P_n(\mathbf{k}_1, \ldots, \mathbf{k}_n) \times e^{-i\mathbf{k}_1\cdot\mathbf{r}_{1n} - \cdots - i\mathbf{k}_{(n-1)}\cdot\mathbf{r}_{(n-1)n}}; \quad \left[\sum_{i=1}^{n}\mathbf{k}_i = \mathbf{0}\right], \tag{A15}$$

where we have very generally defined the n-point spectrum as

$$V_\mu^{n-1}\langle\delta^s(\mathbf{k}_1)\ldots\delta^s(\mathbf{k}_n)\rangle = P_n^s(\mathbf{k}_1,\ldots,\mathbf{k}_n)[\delta^D_{1\ldots n}] \times (2\pi)^3/V_\mu, \quad \text{(A16)}$$

this condition simply arises from the imposed harmonic boundary conditions within our volume: only overlapping waves are constructive. The short-hand notation $[\delta^D_{12\ldots}] \equiv \delta^D(\mathbf{k}_1+\mathbf{k}_2+\ldots)$ has been adopted for the argument of the Dirac delta function. The presence of this term ensures that the sum of k-vectors forms a null vector, $\mathbf{k}_1+\cdots+\mathbf{k}_n=\mathbf{0}$ and we shall refer to this as the closure condition. For the case of $(n=2)$, we have the power spectrum $P_2(\mathbf{k}_1,\mathbf{k}_2)\equiv P(\mathbf{k}_1)$ and for $(n=3)$ we have the bispectrum $P_3(\mathbf{k}_1,\mathbf{k}_2,\mathbf{k}_3)\equiv B(\mathbf{k}_1,\mathbf{k}_2,\mathbf{k}_3)$.

Conversely, the power spectra may also be written as inverse Fourier transforms of the correlation functions:

$$P(\mathbf{k}_1) = \int d^3\mathbf{r}_{12}\xi(\mathbf{r}_{12})e^{i\mathbf{k}_1\cdot\mathbf{r}_{12}}; \quad \text{(A17)}$$

$$B(\mathbf{k}_1,\mathbf{k}_2,\mathbf{k}_3) = \int d^3\mathbf{r}_{13}d^3\mathbf{r}_{23}\zeta(\mathbf{r}_{13},\mathbf{r}_{23})e^{i[\mathbf{k}_1\cdot\mathbf{r}_{13}+\mathbf{k}_2\cdot\mathbf{r}_{23}]}, \quad \text{(A18)}$$

$$P_n(\mathbf{k}_1,\ldots,\mathbf{k}_n) = \int d^3\mathbf{r}_{1n}\ldots d^3\mathbf{r}_{(n-1)n}\xi_n(\mathbf{r}_{1n},\ldots,\mathbf{r}_{(n-1)n}) \times e^{i[\mathbf{k}_1\cdot\mathbf{r}_{1n}+\cdots+\mathbf{k}_{(n-1)}\cdot\mathbf{r}_{(n-1)n}]}. \quad \text{(A19)}$$

From these relations and the properties of the correlation functions, Eqs. (A7)–(A10), we may now infer the corresponding properties for the poly-spectra. Translational invariance in configuration space means that the poly-spectra are invariant under a phase shift to the Fourier density fields. Invariance to rotation of the coordinate frame leads to rotation invariance of the poly-spectra:

$$\begin{aligned} P_n(\mathbf{k}_1,\ldots,\mathbf{k}_n) &= \int d^3[\mathcal{R}\mathbf{r}_{1n}]\ldots d^3[\mathcal{R}\mathbf{r}_{(n-1)n}]\xi_n(\mathcal{R}\mathbf{r}_{1n},\ldots,\mathcal{R}\mathbf{r}_{(n-1)n})e^{i[\mathbf{k}_1^T\mathcal{R}\mathbf{r}_{1n}+\cdots+\mathbf{k}_{(n-1)}^T\mathcal{R}\mathbf{r}_{(n-1)n}]}, \\ &= \int d^3\mathbf{r}_{1n}\ldots d^3\mathbf{r}_{(n-1)n}\xi_n(\mathbf{r}_{1n},\ldots,\mathbf{r}_{(n-1)n})e^{i[\mathbf{r}_{1n}^T\mathcal{R}^T\mathbf{k}_1+\cdots+\mathbf{r}_{(n-1)n}^T\mathcal{R}^T\mathbf{k}_{(n-1)}]} \\ &= P_n(\mathcal{R}^T\mathbf{k}_1,\ldots,\mathcal{R}^T\mathbf{k}_n). \end{aligned} \quad \text{(A20)}$$

Parity invariance and the reality of the configuration space functions leads to the reality of the poly-spectra:

$$\begin{aligned} P_n(\mathbf{k}_1,\ldots,\mathbf{k}_n) &= P_n(-\mathbf{k}_1,\ldots,-\mathbf{k}_n) \\ &= [P_n(\mathbf{k}_1,\ldots,\mathbf{k}_n)]^*, \end{aligned} \quad \text{(A21)}$$

where the $*$ corresponds to complex conjugation. Many of these properties simplify the analysis in the main text.

APPENDIX B: CALCULATIONAL DETAILS

1. The NFW density profile with the Bullock *et al.* normalization

As described in Sec. III B to compute the redshift-space density profile we require a model for the real-space density profile $\rho(r)$ and a model for the 1-point velocity distribution function of particles in a halo. For the density profile we adopt the Navarro-Frenk-White (NFW) model [89]:

$$\rho(r) = \rho_c[y(1+y)^2]^{-1}; \qquad y \equiv r/r_c. \quad \text{(B1)}$$

This model is fully determined by two parameters, ρ_c and r_c, a characteristic density, and radius. These two parameters are not independent, but are related by the mass enclosed:

$$\rho_c = \frac{\bar\rho\Delta_{\rm vir}c^3/3}{\ln(1+c)-c/(1+c)}; \qquad c \equiv \frac{r_{\rm vir}}{r_c}, \quad \text{(B2)}$$

where c is the concentration parameter and is the ratio of the virial radius to the characteristic radius. The virial radius is the boundary layer within which all particles have undergone violent nonlinear relaxation. It is taken to be specified through

$$M_{\rm vir} = \tfrac{4}{3}\pi r_{\rm vir}^3\Delta_{\rm vir}\bar\rho, . \quad \text{(B3)}$$

$\Delta_{\rm vir}$ is the density contrast for virialization, which may be estimated from the spherical collapse model. For flat universes with a cosmological constant a good fit to the functional form is provided by [90]

$$\begin{aligned} \Delta_{\rm vir} &= [(18\pi^2+82x-39x^2]/\Omega(a); \\ x &\equiv [\Omega(a)-1]. \end{aligned} \quad \text{(B4)}$$

To obtain the concentration parameter as a function of mass we follow the model of Bullock *et al.* [91]. For this we have

$$c = K\frac{a}{a_c(M_{\rm vir})}, \quad \text{(B5)}$$

where we take $K=3.0$ and where $a_c(M_{\rm vir})$ is the collapse expansion factor for a halo of mass $M_{\rm vir}$. The collapse expansion factor for a halo of mass M may be determined through solving the relation

$$\frac{D_1(a_c)}{D_1(a_0)}\sigma(FM_{\rm vir}, a_0) = \delta_c, \tag{B6}$$

where $F = 0.001$ is taken as a fixed fraction of the initial mass, $D(a)$ is the linear theory growth factor at epoch a. The parameter $\delta_c = 1.686$ is the linearly extrapolated density threshold for collapse from the spherical collapse model, where we ignore the slight dependence on cosmology [92]. As was shown by [91] this model provides a very good description of the ensemble average properties of dark matter haloes. More sophisticated models may be constructed that take into account that haloes are more complicated, e.g. a halo of mass M drawn at random from the ensemble will have a concentration parameter that is drawn from a probability distribution of possible concentrations. In addition one may include substructure [93] or halo triaxiality [20,70]. However, we shall leave these additional embellishments for future study.

2. Conversion between Sheth and Tormen and Bullock *et al.* mass definitions

The definitions of halo mass that are used in the Sheth and Tormen mass function and the Bullock *et al.* model for the density profile are inconsistent. We recall that the Sheth and Tormen halo mass is defined:

$$M_{\rm ST} = \tfrac{4}{3}\pi r_{\rm ST}^3 200\bar{\rho}. \tag{B7}$$

We resolve this inconsistency using the methodology of [70], which briefly is as follows: For a given halo of the NFW type, the physical values of the characteristic density and radius are independent of our specific choice of halo mass. Using the relation for the physical density as a constant we arrive at the mapping

$$\left(\frac{c_{\rm vir}}{c_{\rm ST}}\right)^3 = \frac{200}{\Delta_{\rm vir}}\left[\frac{\ln(1+c_{\rm vir}) - c_{\rm vir}/(1+c_{\rm vir})}{\ln(1+c_{\rm ST}) - c_{\rm ST}/(1+c_{\rm ST})}\right]. \tag{B8}$$

Thus if we take a Bullock *et al.* mass and derive the appropriate $c_{\rm vir}$ we may then solve the above expression to find $c_{\rm ST}$. Following this we may then obtain the corresponding Sheth and Tormen mass through application of the relation,

$$M_{\rm ST} = \frac{200}{\Delta_{\rm vir}}\left(\frac{c_{\rm ST}}{c_{\rm vir}}\right)^3 M_{\rm vir}. \tag{B9}$$

3. 1-point velocity distribution profile

For the 1D velocity distribution function we adopt the standard Maxwellian distribution [45–47,94]:

$$\mathcal{V}[u_z|\sigma_{\rm 1D}(M_{\rm vir})]du_z = \frac{1}{\sqrt{2\pi}\sigma_{\rm 1D}}\exp\left[-\frac{u_z^2}{2\sigma_{\rm 1D}^2}\right]du_z, \tag{B10}$$

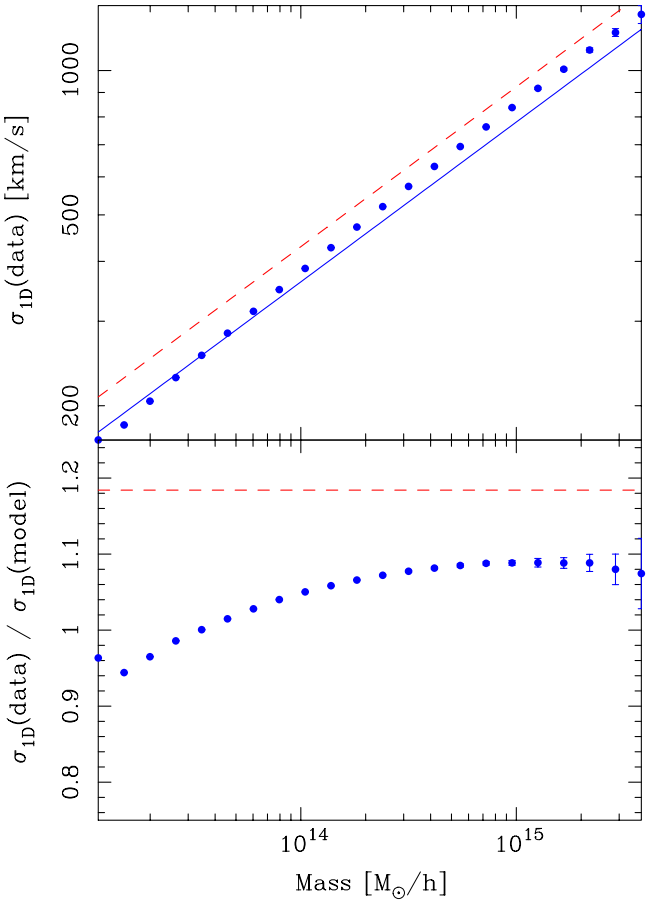

FIG. 6 (color online). Mass vs 1D velocity dispersion measured for FoF haloes in simulations. Points show mean and 1-sigma errors for measurements from the numerical simulations. The solid and dash line shows the predictions from Eq. (B12) with $\epsilon = \{0.76, 1.0\}$. The bottom panel shows the ratio of the data with respect to the $\epsilon = 0.76$ model.

where $\sigma_{\rm 1D}$ is the 1D velocity dispersion. For haloes that possess an isothermal density distribution, this quantity is related to the halo circular velocity (V_c) through the following relation [95]:

$$\sigma_{\rm 1D}^2(M_{\rm vir}) = \epsilon V_c^2/2; \qquad V_c^2 = \frac{GM_{\rm vir}}{r_{\rm vir}}. \tag{B11}$$

Note that we have included a parameter ϵ into Eq. (B11), this may be used to account for the fact that the relation is only approximately true for the NFW density profile model. It also serves the further purpose of allowing us to turn off the fingers-of-god through setting $\epsilon \to \eta \ll 1$. As discussed in Sec. VI B and shown in Fig. 6 $\epsilon = 0.76$ provides a reasonable fit to the velocity dispersion mass relation from simulations. On combining the above relations we have

$$\sigma_{\rm 1D}^2(M_{\rm vir}) = \frac{100\epsilon}{2}\Omega_m(a)[H(a)r_{\rm vir}]^2. \quad \text{(B12)}$$

Notice that the ratio $\sigma_{\rm 1D}(M_{\rm vir})/r_{\rm vir}$ is independent of halo mass. One immediate consequence of this is that in redshift space the ratio of the line-of-sight projection of particles in a halo compared to the transverse length will be a constant, $\sigma_{\rm 1D}/(Hr_{\rm vir}) \sim 3$, regardless of mass. In other words, FOGs lead to density profiles which are self-similar. In our analysis we take $\epsilon = 0.76$ (see Fig. 6). Finally, the Fourier transform of the velocity distribution is

$$\mathcal{V}(\mu_1 k_1) = \exp\{-\tfrac{1}{2}[k_1\mu_1\sigma_{\rm 1D}(M_{\rm vir})]^2\}. \quad \text{(B13)}$$

APPENDIX C: EULERIAN PT AND HALO-PT KERNELS

The first two symmetrized Eulerian PT kernels for the density and divergence of the velocity field are [6]:

$$F_{1,2} = \frac{5}{7} + \frac{\mu_{12}}{2}\left[\frac{q_1}{q_2} + \frac{q_2}{q_1}\right] + \frac{2(\mu_{12})^2}{7}; \quad \text{(C1)}$$

$$G_{1,2} = \frac{3}{7} + \frac{\mu_{12}}{2}\left[\frac{q_1}{q_2} + \frac{q_2}{q_1}\right] + \frac{4(\mu_{12})^2}{7}, \quad \text{(C2)}$$

where $F_{1,\ldots,j} \equiv F_j(\mathbf{q}_1,\ldots,\mathbf{q}_j)$ and where $\mu_{12} \equiv \mathbf{q}_1\cdot\mathbf{q}_2/q_1q_2$.

The Halo-PT kernels, symmetrized in all of their arguments, may be written in terms of the Eulerian PT kernels up to 2nd order as [38]:

$$F_0^{\rm hc} = b_0(M); \quad \text{(C3)}$$

$$F_1^{\rm hc} = b_1(M)W(|\mathbf{k}|R)F_1; \quad \text{(C4)}$$

$$F_{1,2}^{\rm hc} = b_1(M)W(|\mathbf{k}|R)F_{1,2} + \frac{b_2(M)}{2}W(|\mathbf{q}_1|R)W(|\mathbf{q}_2|R)F_1F_2, \quad \text{(C5)}$$

where $F_{1,\ldots,j}^{\rm hc} \equiv F_j^{\rm hc}(\mathbf{q}_1,\ldots,\mathbf{q}_j|M,R)$ and where $\mathbf{k} = \mathbf{q}_1 + \cdots + \mathbf{q}_j$.

APPENDIX D: ROTATION MATRIX

Owing to there being several equivalent ways to define the Euler angles and hence the rotation matrix $\mathcal{R}(\gamma_1,\gamma_2,\gamma_3)$, we make explicit our adopted choice. The angles are defined as follows: γ_1 describes a rotation of the coordinate system around the z-axis; γ_2 a rotation around the new y'-axis; and γ_3 a rotation around the new z''-axis ([96]). Thus, the components of any vector $\mathbf{k}$ specified in some initial Cartesian system can be transformed into the scalar components of the new rotated basis vectors through $\mathbf{k}' = \mathcal{R}(\gamma_1,\gamma_2,\gamma_3)\mathbf{k}$. The $z - y' - z''$ rotation matrix is [96]:

$$\mathcal{R}(\gamma_1,\gamma_2,\gamma_3) \equiv \begin{pmatrix} [C\gamma_2C\gamma_1C\gamma_3 - S\gamma_1S\gamma_3] & [C\gamma_2S\gamma_1C\gamma_3 + C\gamma_1S\gamma_3] & -S\gamma_2C\gamma_3 \\ [-C\gamma_2C\gamma_1S\gamma_3 - S\gamma_1C\gamma_3] & [-C\gamma_2S\gamma_1S\gamma_3 + C\gamma_1C\gamma_3] & S\gamma_2S\gamma_3 \\ S\gamma_2C\gamma_1 & S\gamma_2S\gamma_1 & C\gamma_2 \end{pmatrix}, \quad \text{(D1)}$$

and we employed the economic notation $Cx = \cos x$ and $Sx = \sin x$.

APPENDIX E: REDSHIFT-SPACE POWER SPECTRUM MONOPOLE IN THE HALO MODEL

The redshift-space power spectrum of tracer particles α can be written in the linear halo model as

$$P_\alpha^s(\mathbf{k}) = P_{\alpha,\rm 1H}^s(\mathbf{k}) + P_{\alpha,\rm 2H}^s(\mathbf{k}): \quad \text{(E1)}$$

$$P_{\alpha,\rm 1H}^s(\mathbf{k}) = \frac{P_{\alpha,\rm 1H}^s(\mathbf{k}|R)}{[W(k|R)]^2} = \frac{1}{\bar\rho_\alpha^2}\int dMn(M)[W_\alpha]^2|U^s(\mathbf{k}|M)|^2, \quad \text{(E2)}$$

$$P_{\alpha,\rm 2H}^s(\mathbf{k}) = \frac{P_{\alpha,\rm 2H}^s(\mathbf{k}|R)}{[W(k|R)]^2} = \frac{1}{\bar\rho_\alpha^2}\int\prod_{i=1}^{2}\{dM_in(M_i)[W_\alpha]_iU^s(\mathbf{k}|M_i)\} \times \frac{P_{\rm hc}^s(\mathbf{k}|M_1,M_2,R)}{[W(k|R)]^2}. \quad \text{(E3)}$$

At linear order the redshift-space power spectrum of halo seeds is

$$P_{\rm hc}^s(\mathbf{k}|M_1,M_2,R) = Z_1(\mathbf{k}|M_1,R)Z_1(\mathbf{k}|M_1,R)P_{11}(k) = [W(kR)]^2b_1(M_1)b_1(M_2)P_{11}(k) \times\{1 + \mu^2[\beta_1 + \beta_2] + \beta_1\beta_2\mu^4\}; \quad \beta_i \equiv \frac{f(\Omega)}{b_1(M_i)}, \quad \text{(E4)}$$

where $b_0 = 0$ can be seen from the fact that the halo and density fluctuation fields are by definition mean zero

fields and recalling that at linear order $\langle \delta_1^h(r|M)\rangle = b_0(M) + b_1(M)\langle\delta_1(r|M)\rangle$. The redshift-space power spectrum monopole is thus

$$\hat{P}^{\,s}_{\alpha,1\mathrm{H}}(k) = \frac{1}{\bar{\rho}_\alpha^2}\int dM n(M) \times [W_\alpha]^2 |U^\alpha(k|M)|^2 \mathcal{R}^{(0)}_{1,2}[k\sigma(M)], \quad \text{(E5)}$$

$$P^s_{\alpha,2\mathrm{H}}(k) = \frac{1}{\bar{\rho}_\alpha^2}\int \prod_{i=1}^{2}\{dM_i n(M_i) b_1(M_i) \times [W_\alpha]_i U(k|M_i)\}\mathcal{R}^{(0)}_{2,2}[k\sigma_2(M)], \quad \text{(E6)}$$

where we have defined the redshift-space multipole factors

$$\mathcal{R}^{(l)}_{1,n}[a] = \frac{2l+1}{2}\int_{-1}^{1} d\mu \mathcal{P}_l(\mu)\exp[-a^2\mu^2]; \quad \text{(E7)}$$

$$\mathcal{R}^{(l)}_{2,n}[b] = \frac{2l+1}{2}\int_{-1}^{1} d\mu \mathcal{P}_l(\mu)[1 + A\mu^2 + B\mu^4] \times \exp[-b^2\mu^2]. \quad \text{(E8)}$$

Here $a^2 \equiv nk^2\sigma^2(M)/2$, $b^2 \equiv k^2[\sigma^2(M_1) + \cdots + \sigma^2(M_n)]/2$ we have set $A = \beta_1 + \beta_2$ and $B = \beta_1\beta_2$, and we have assumed our Gaussian model for the 1-pt velocity distribution function from Eq. (B13). Thus, the monopole [$l = 0$; $\mathcal{P}_0(\mu) = 1$] moments are

$$\mathcal{R}^{(0)}_{1,n}(a) = \frac{\sqrt{\pi}}{2}\frac{\mathrm{erf[a]}}{a}; \quad \text{(E9)}$$

$$\mathcal{R}^{(0)}_{2,n}(b) = \frac{\mathcal{R}^{(0)}_{1,n}(b)}{4b^4}[4b^4 + 2b^2A + 3B] - \frac{\exp(-b^2)}{4b^4} \times [2b^2(A+B) + 3B]. \quad \text{(E10)}$$

Our expression differs from that of [45,46], but is consistent with the formulation of [47]. For further discussion and comments on this subject, and for an evaluation of the power spectrum to higher order in the halo-PT series, see [48].

Note that when $a \ll 1$ and $b \ll 1$, then

$$\mathcal{R}^{(0)}_{1,n}(a) = \exp(-a^2)\sum_{j=0}^{\infty}\frac{2^j}{(2j+1)!!}a^{2j} = \sum_{j=0}^{\infty}\frac{(-1)^j}{j!(2j+1)}a^{2j}, \quad \text{(E11)}$$

$$\begin{aligned}\mathcal{R}^{(0)}_{2,n}(b) &= \frac{\exp(-b^2)}{4b^4}\left([4b^4 + 2b^2A + 3B]\sum_{j=0}^{\infty}\frac{2^j}{2j+1)!!}b^{2j} - 2b^2(A+B) - 3B\right)\\ &= \frac{\exp(-b^2)}{4b^4}\left([4b^4 + 2b^2A + 3B]\left[1 + \frac{2b^2}{3} + \frac{4b^4}{15} + \frac{8b^6}{105} + \ldots\right] - 2b^2(A+B) - 3B\right)\\ &= \exp(-b^2)\left(1 + \frac{A}{3} + \frac{B}{5} + \frac{2b^2}{3}\left[1 + \frac{A}{5} + \frac{3B}{35}\right] + \frac{4b^4}{15}\left[1 + \frac{A}{7} + \frac{B}{21}\right] + \ldots\right)\\ &\approx \left(1 + \frac{\beta_1+\beta_2}{3} + \frac{\beta_1\beta_2}{5}\right)\end{aligned} \quad \text{(E12)}$$

reducing to the Kaiser formula on large scales [40].

APPENDIX F: IMPACT OF SHOT NOISE ON THE REDUCED BISPECTRUM

It is of interest to consider how standard shot noise and also the halo model effective shot-noise terms impact the reduced bispectrum. On large scales Q^{HM} can be written:

$$Q^{\mathrm{HM}} = \frac{B^{\mathrm{PT}} + \frac{1}{\bar{n}_{2\mathrm{H,B}}}[P_1 + P_2 + P_3] + \frac{1}{\bar{n}^2_{1\mathrm{H,B}}}}{(P_1 + \frac{1}{\bar{n}_{1\mathrm{H,P}}})(P_2 + \frac{1}{\bar{n}_{1\mathrm{H,P}}}) + 2\,\mathrm{cyc}}, \quad \text{(F1)}$$

where we have added a subscript P or B to distinguish between shot-noise terms from the halo model power spectrum and bispectrum, respectively.

In the low-sampling limit $\bar{n}_{\mathrm{H}}P \ll 1$, we have the result that

$$Q^{\mathrm{HM}} = \frac{1}{3}\left[\frac{\langle[W_\alpha]^3\rangle\langle[W_\alpha]\rangle}{\langle[W_\alpha]^2\rangle^2}\right] \quad \text{(F2)}$$

for the case of standard shot noise, the term in square brackets is unity, and we have $Q^{\mathrm{d}} = 1/3$, where superscript d means discrete.

In the high sampling limit, $\bar{n}_{\mathrm{H}}P \gg 1$, the denominator in Eq. (F1) becomes

$$\approx \frac{1}{Q_{\mathrm{fac}}}\left[1 - \frac{2}{\bar{n}_{1\mathrm{H},P}}\frac{P_1+P_2+P_3}{Q_{\mathrm{fac}}} - \frac{3}{\bar{n}^2_{1\mathrm{H},P}}\frac{1}{Q_{\mathrm{fac}}}\right], \quad \text{(F3)}$$

where $Q_{\mathrm{fac}} \equiv P_1P_2 + 2\,\mathrm{cyc}$ and where we have treated the last two terms in the square brackets as small quantities, relative to Q_{fac}. On replacing this in Eq. (F1), we find

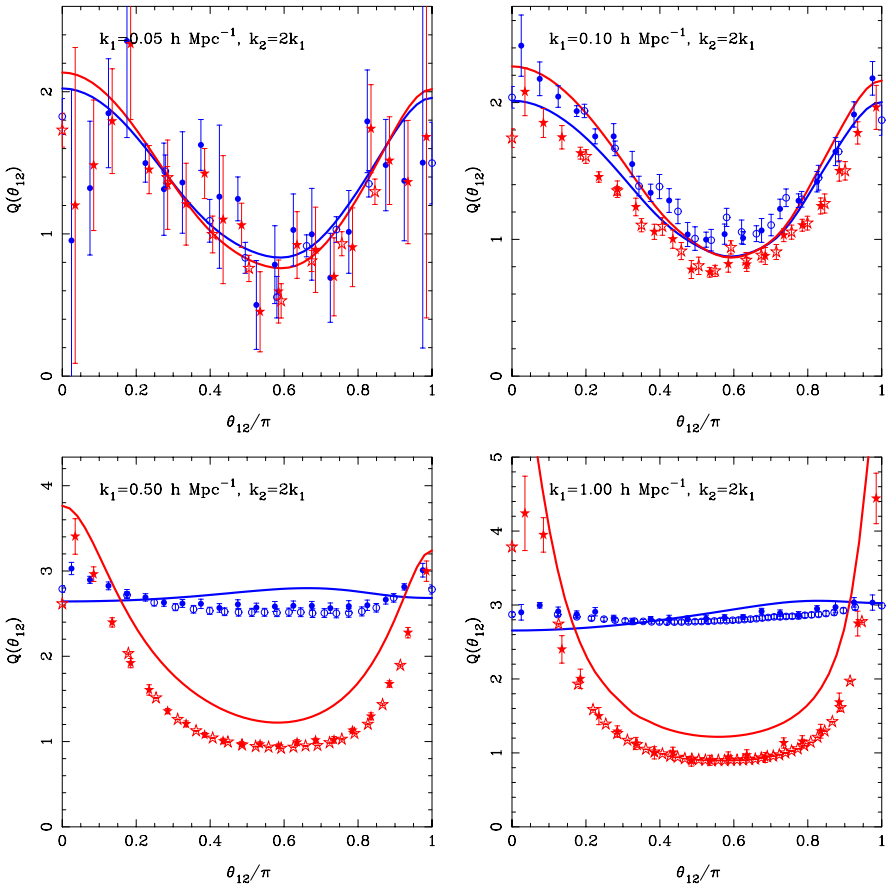

FIG. 7 (color online). Comparison of the reduced bispectrum estimates obtained from the method presented in Sec. VI C with those obtained from the "full sampling code" of [88]. As in Fig. 5, our results are represented by solid symbols, and those from the alternate method are denoted by open symbols. Again, errors are on the mean and real and redshift-space estimates from the same code have been slightly offset in the x-axis to enhance clarity.

$$Q^{\rm HM} - Q^{\rm PT} = \frac{P_1 + P_2 + P_3}{Q_{\rm fac}}\left[\frac{1}{\bar{n}_{2{\rm H},B}} - \frac{2}{\bar{n}_{1{\rm H},P}}(1 + Q^{\rm PT})\right] + \frac{1}{Q_{\rm fac}}\left[\frac{1}{\bar{n}^2_{1{\rm H},B}} - \frac{3}{\bar{n}^2_{1{\rm H},P}}(1 + Q^{\rm PT})\right]. \quad \text{(F4)}$$

We can also use the above expression to derive the effect of standard shot noise on the reduced bispectrum, by simply considering all of the number density terms to be identical, and this gives

$$Q^{\rm d} - Q^{\rm PT} = -\frac{(P_1 + P_2 + P_3)}{\bar{n} Q_{\rm fac}}(1 + 2Q^{\rm PT}) - \frac{1}{\bar{n}^2 Q_{\rm fac}}(2 + 3Q^{\rm PT}). \quad \text{(F5)}$$

Considering standard shot noise first, in Eq. (F5), we see that the effect of discretization of matter is always to reduce the value of Q^d relative to $Q^{\rm PT}$ (the continuum limit case). Considering now the halo model, in Eq. (F4), we see that the difference between this and $Q^{\rm PT}$ depends on the sign of the quantities in square brackets. For dark matter, the first term can be seen to be negative, since $\bar{n}_{2{\rm H,B}} = \bar{n}_{1{\rm H,P}}$. However, the sign of the second term is not as obvious to deduce. If it is negative, then the effect is as for standard shot noise; on the other hand, if the reverse is true, then $Q^{\rm d} > Q^{\rm PT}$.

Lastly, the configuration dependence of $Q^{\rm d} - Q^{\rm PT}$ in the standard shot-noise case can be understood from the following: if we assume that all k-vectors are larger than the turnover scale in the power spectrum, then the quantity $Q_{\rm fac}(\theta_{12} = 1) > Q_{\rm fac}(\theta_{12} = 0)$. This implies that the difference is largest when k_1 and k_2 are parallel.

APPENDIX G: BISPECTRUM CODE COMPARISON

In this appendix we compare results from our recipe for estimating the reduced bispectrum, presented in Sec. VI C, with those obtained from an independent prescription used by one of us over the years, e.g. [88], which uses full sampling of all k-space triangles on the Fourier grid. The two methods are very similar, but some subtle differences exist, these can be summarized: for the "full sampling code":

(1) B is estimated in linear bins of thickness a $1 \times k_f$ for $k = 0.05$, $0.1[h\ \mathrm{Mpc}^{-1}]$ and $4 \times k_f$ for the case $k = 0.5$, $1.0[h\ \mathrm{Mpc}^{-1}]$ ($k_f = 2\pi/L$); whereas for our code estimates are made in $\Delta \log_{10} k$ bins of thickness 0.05;
(2) the configuration dependence of B is estimated as a linear function of k_3, whereas for our code it is estimated as a linear function of θ_{12};
(3) all of the available independent k-modes are used, whereas we sub- or oversample modes from the available set depending on the number of available modes;
(4) Q is constructed from estimates of B and P in a post-processing fashion, whereas we estimate Q on the fly for each triangle that is used in the estimate.

Figure 7 shows the results of this comparison. The solid symbols denote our results, and the corresponding open symbols denote the results from the "full sampling code." Overall we find very good agreement between both methods. On the largest scales that we have considered, $k_1 = 0.05h\ \mathrm{Mpc}^{-1}$, it appears that our method is a factor of 2–3 times more noisy than that of R. Scoccimarro, however we have a factor of 2 more bins in θ_{12}, which accounts for some of this discrepancy. On smaller scales $k_1 \geq 0.1h\ \mathrm{Mpc}^{-1}$ the estimates are of comparable quality, with ours being slightly more noisy. The discrepancy on large scales owes to the fact that we have subsampled triangles from the possible set; this can be mitigated by oversampling from the number of available modes. On smaller scales the benefits of our approach are that we may obtain a high accuracy estimate without requiring all of the triangles and this also has the practical advantage of keeping the computational time tolerably low.

[1] M. Tegmark (SDSS Collaboration), Astrophys. J. **606**, 702 (2004).
[2] S. Cole (2dFGRS Collaboration), Mon. Not. R. Astron. Soc. **362**, 505 (2005).
[3] D. J. Eisenstein (SDSS Collaboration), Astrophys. J. **633**, 560 (2005).
[4] M. Tegmark (SDSS Collaboration), Phys. Rev. D **74**, 123507 (2006).
[5] D. Spergel (WMAP Collaboration), Astrophys. J. Suppl. Ser. **170**, 377 (2007).
[6] F. Bernardeau, S. Colombi, E. Gaztañga, and R. Scoccimarro, Phys. Rep. **367**, 1 (2002).
[7] E. Sefusatti and R. Scoccimarro, Phys. Rev. D **71**, 063001 (2005).
[8] J. Fry and E. Gaztañaga, Astrophys. J. **413**, 447 (1993).
[9] J. A. Frieman and E. Gaztañaga, Astrophys. J. **425**, 392 (1994).
[10] J. N. Fry, Phys. Rev. Lett. **73**, 215 (1994).
[11] E. Sefusatti, M. Crocce, S. Pueblas, and R. Scoccimarro, Phys. Rev. D **74**, 023522 (2006).
[12] J. N. Fry and R. J. Scherrer, Astrophys. J. **429**, 36 (1994).
[13] E. Gaztañaga and P. Fosalba, Mon. Not. R. Astron. Soc. **301**, 524 (1998).
[14] R. Scoccimarro, E. Sefusatti, and M. Zaldarriaga, Phys. Rev. D **69**, 103513 (2004).
[15] E. Sefusatti and E. Komatsu, Phys. Rev. D **76**, 083004 (2007).
[16] F. Bernardeau, arXiv:astro-ph/0409224.
[17] A. Shirata, Y. Suto, C. Hikage, T. Shiromizu, and N. Yoshida, Phys. Rev. D **76**, 044026 (2007).
[18] B. Jain and P. Zhang, arXiv:0709.2375.
[19] R. Scoccimarro (unpublished).
[20] R. E. Smith, P. I. R. Watts, and R. K. Sheth, Mon. Not. R. Astron. Soc. **365**, 214 (2006).
[21] W. Saunders (PSCz Collaboration), Mon. Not. R. Astron. Soc. **317**, 55 (2000).
[22] M. Colless (2dFGRS Collaboration), Mon. Not. R. Astron. Soc. **328**, 1039 (2001).
[23] D. G. York (SDSS Collaboration), Astron. J. **120**, 1579 (2000).
[24] D. P. Schneider (SDSS Collaboration), Astron. J. **134**, 102 (2007).
[25] I. Kayo, Y. Suto, R. C. Nichol, J. Pan, I. Szapudi, A. J. Connolly, J. Gardner, B. Jain, G. Kulkarni, T. Matsubara, R. K. Sheth, A. S. Szalay, and J. Brinkmann, Publ. Astron. Soc. Jpn. **56**, 415 (2004).
[26] Y. P. Jing and G. Böerner, Astrophys. J. **607**, 140 (2004).
[27] Y. Wang, X. Yang, H. J. Mo, F. C. van den Bosch, and Y-Q. Chu, Mon. Not. R. Astron. Soc. **353**, 287 (2004).
[28] E. Gaztanaga, P. Norberg, C. M. Baugh, and D. J. Croton, Mon. Not. R. Astron. Soc. **364**, 620 (2005).
[29] R. C. Nichol (SDSS Collaboration), Mon. Not. R. Astron. Soc. **368**, 1507 (2006).
[30] G. Kulkarni, R. Nichol, R. K. Sheth, H.-J. Seo, D. J. Eisenstein, and A. Gray, Mon. Not. R. Astron. Soc. **378**, 1196 (2007).
[31] R. Scoccimarro, H. Feldman, J. Frieman, and J. N. Fry, Astrophys. J. **546**, 652 (2001).
[32] H. Feldman, J. Frieman, J. N. Fry, and R. Scoccimarro, Phys. Rev. Lett. **86**, 1434 (2001).
[33] L. Verde, A. F. Heavens (The 2dfGRS Collaboration), Mon. Not. R. Astron. Soc. **335**, 432 (2002).
[34] T. Nishimichi, I. Kayo, C. Hikage, K. Yahata, A. Taruya, Y.-P. Jing, R. K. Sheth, and Y. Suto, Publ. Astron. Soc. Jpn. **59**, 93 (2007).
[35] R. Scoccimarro, H. M. P. Couchman, and J. A. Frieman, Astrophys. J. **517**, 531 (1999).
[36] E. Gaztañaga and R. Scoccimarro, Mon. Not. R. Astron. Soc. **361**, 824 (2005).
[37] L. Verde, A. F. Heavens, S. Matarrese, and L. Moscardini, Mon. Not. R. Astron. Soc. **300**, 747 (1998).
[38] R. E. Smith, R. Scoccimarro, and R. K. Sheth, Phys. Rev.

D 75, 063512 (2007).
[39] M. Davis and P. J. E. Peebles, Astrophys. J. **267**, 465 (1983).
[40] N. Kaiser, Mon. Not. R. Astron. Soc. **227**, 1 (1987).
[41] A. J. S. Hamilton, *The Evolving Universe* (Kluwer Academic, Dordrecht, 1998), p. 185.
[42] R. Scoccimarro, Phys. Rev. D **70**, 083007 (2004).
[43] A. Cooray and R. K. Sheth, Phys. Rep. **372**, 1 (2002).
[44] R. K. Sheth, A. Diaferio, L. Hui, and R. Scoccimarro, Mon. Not. R. Astron. Soc. **326**, 463 (2001).
[45] M. White, Mon. Not. R. Astron. Soc. **321**, 1 (2001).
[46] U. Seljak, Mon. Not. R. Astron. Soc. **325**, 1359 (2001).
[47] X. Kang, Y. P. Jing, H. J. Mo, and G. Böerner, Mon. Not. R. Astron. Soc. **336**, 892 (2002).
[48] R. E. Smith *et al.* (unpublished).
[49] A. J. Benson, S. Cole, C. S. Frenk, C. M. Baugh, and C. G. Lacey, Mon. Not. R. Astron. Soc. **311**, 793 (2000).
[50] U. Seljak, Mon. Not. R. Astron. Soc. **318**, 203 (2000).
[51] J. A. Peacock and R. E. Smith, Mon. Not. R. Astron. Soc. **318**, 1144 (2000).
[52] R. Scoccimarro, R. K. Sheth, L. Hui, and B. Jain, Astrophys. J. **546**, 20 (2001).
[53] A. Berlind and D. Weinberg, Astrophys. J. **575**, 587 (2002).
[54] R. E. Smith, J. A. Peacock, A. Jenkins, S. D. M. White, C. S. Frenk, F. R. Pearce, P. A. Thomas, G. Efstathiou, and H. M. P. Couchman, Mon. Not. R. Astron. Soc. **341**, 1311 (2003).
[55] M. Crocce and R. Scoccimarro, Phys. Rev. D **77**, 023533 (2008).
[56] M. C. Neyrinck and I. Szapudi, Mon. Not. R. Astron. Soc. **384**, 1221 (2008).
[57] U. Seljak and M. Zaldarriaga, Astrophys. J. **469**, 437 (1996).
[58] J. Tinker, Mon. Not. R. Astron. Soc. **374**, 477 (2007).
[59] R. Scherrer and E. Bertschinger, Astrophys. J. **381**, 349 (1991).
[60] M. Takada and B. Jain, Mon. Not. R. Astron. Soc. **340**, 580 (2003).
[61] W. Press and P. Schechter, Astrophys. J. **187**, 425 (1974).
[62] J. R. Bond, S. Cole, N. Kaiser, and G. Efstathiou, Astrophys. J. **379**, 440 (1991).
[63] R. K. Sheth and G. Tormen, Mon. Not. R. Astron. Soc. **308**, 119 (1999).
[64] R. K. Sheth, H.-J. Mo, and B. Tormen, Mon. Not. R. Astron. Soc. **323**, 1 (2001).
[65] A. Jenkins, C. S. Frenk, S. D. M. White, J. Colberg, S. Cole, A. Evrard, H. Couchman, and N. Yoshida, Mon. Not. R. Astron. Soc. **321**, 372 (2001).
[66] M. S. Warren, K. Abazajian, D. E. Holz, and L. Teodoro, Astrophys. J. **646**, 881 (2006).
[67] D. Reed, R. Bower, C. S. Frenk, A. Jenkins, and T. Theuns, Mon. Not. R. Astron. Soc. **374**, 2 (2007).
[68] For example: substructures will produce localized features in the phase-space distribution [97,98]; a global asymmetry of the underlying potential, generated through the anisotropic accretion of matter, will distort the velocity structure of the phase space into a 6-D triaxial ellipsoid [99].
[69] Kang *et al.* [47] show that if one considers the ensemble average of the phase-space distribution for haloes, then $\mathcal{V}(\mu k|M)$ is reasonably well described by a Maxwellian. This result was further corroborated by [100], who computed $\mathcal{V}(\mu k|M)$ for a halo with an NFW density profile [89] by solving the Jeans Equation. They found that it was well approximated by a Maxwellian. But, see also [87] for a recent exploration of the halo phase-space distributions.
[70] R. E. Smith and P. I. R. Watts, Mon. Not. R. Astron. Soc. **360**, 203 (2005).
[71] E. Hivon, F. R. Bouchet, S. Colombi, and R. Juszkiewicz, Astron. Astrophys. **298**, 643 (1995).
[72] P. McDonald, Phys. Rev. D **74**, 103512 (2006).
[73] P. J. E. Peebles, *The Large-Scale Structure of the Universe* (Princeton University, Princeton, NJ, 1980).
[74] R. Scoccimarro, S. Colombi, J. N. Fry, J. A. Frieman, E. Hivon, and A. Melott, Astrophys. J. **517**, 531 (1999).
[75] R. Scoccimarro, Mon. Not. R. Astron. Soc. **299**, 1097 (1998).
[76] M. Crocce, S. Pueblas, and R. Scoccimarro, Mon. Not. R. Astron. Soc. **373**, 369 (2006).
[77] V. Springel, Mon. Not. R. Astron. Soc. **364**, 1105 (2005).
[78] R. W. Hockney and J. W. Eastwood, *Computer Simulations Using Particles* (McGraw-Hill, New York, 1981).
[79] M. Frigo and S. G. Johnson, http://www.fftw.org/ (2007).
[80] Y. P. Jing, Astrophys. J. **620**, 559 (2005).
[81] D. J. Eisenstein and W. Hu, Astrophys. J. **496**, 605 (1998).
[82] A. Meiksin, M. White, and J. A. Peacock, Mon. Not. R. Astron. Soc. **304**, 851 (1999).
[83] R. E. Smith, R. Scoccimarro, and R. K. Sheth, Phys. Rev. D **77**, 043525 (2008).
[84] A. Neto *et al.*, Mon. Not. R. Astron. Soc. **381**, 1450 (2007).
[85] A. Cooray and W. Hu, Astrophys. J. **554**, 56C (2001).
[86] C. Lacey and S. Cole, Mon. Not. R. Astron. Soc. **281**, 716 (1996).
[87] A. J. Cuesta, F. Prada, A. Klypin, and M. Moles, arXiv:0710.5520 [Mon. Not. R. Astron. Soc. (to be published)].
[88] R. Scoccimarro, Astrophys. J. **544**, 597 (2000).
[89] J. Navarro, C. S. Frenk, and S. D. M. White, Astrophys. J. **490**, 493 (1997).
[90] G. Bryan and M. Norman, Astrophys. J. **495**, 80 (1998).
[91] J. Bullock, T. Kolatt, Y. Sigad, R. Somerville, A. Kravtsov, A. Klypin, J. Primack, and A. Dekel, Mon. Not. R. Astron. Soc. **321**, 559 (2001).
[92] O. Lahav, P. Lilje, J. Primack, and M. Rees, Mon. Not. R. Astron. Soc. **251**, 128 (1991).
[93] R. K. Sheth and B. Jain, Mon. Not. R. Astron. Soc. **345**, 529 (2003).
[94] R. K. Sheth, Mon. Not. R. Astron. Soc. **279**, 1310 (1996).
[95] J. Binney and S. Tremaine, *Galactic Dynamics* (Princeton University, Princeton, NJ, 1988).
[96] J. Mathews and R. L. Walker, *Mathematical Methods of Physics* (Benjamin, New York, 1970).
[97] B. Moore, T. Quinn, F. Governato, J. Stadel, and G. Lake, Mon. Not. R. Astron. Soc. **310**, 1147 (1999).
[98] A. Klypin, S. Gottlber, A. Kravtsov, and A. M. Khokhlov, Astrophys. J. **516**, 530 (1999).
[99] Y. P. Jing and Y. Suto, Astrophys. J. **574**, 538 (2002).
[100] T. Kuwabara, A. Taruya, and Y. Suto, Publ. Astron. Soc. Jpn. **54**, 503 (2002).